國立交通大學

電子工程學系 電子研究所碩士班

碩士論文

鎳鍺化物與N型鍺接面摻雜析離對於蕭基位障的影響:透過第一原理計算

Schottky Barrier Height of the NiGe/n-type Ge Contact with Dopant Segregation: A First-principles Study

研究生 ： 林翰奇

指導教授 ： 崔秉鉞 教授

共同指導教授 ： 林炯源 教授

中華民國一０二年九月

鎳鍺化物與N型鍺接面摻雜析離對於蕭基位障的影響：透過第一原理計算

Schottky Barrier Height of the NiGe/n-type Ge Contact with Dopant Segregation: A First-principles Study

研究生 ： 林翰奇　Student : Han-Chi Lin

指導教授 ：崔秉鉞　Advisor : Bing-Yue Tsui

共同指導教授 ： 林炯源　Co-advisor : Chiung-Yuan Lin

國立交通大學

電子工程學系 電子研究所

碩士論文

A Thesis

Submitted to Department of Electronics Engineering and Institute of Electronics

College of Electrical Engineering and Computer Engineering

National Chiao Tung University

in Partial Fulfillment of the Requirement

for the Degree of Master of Science

in

Electronic Engineering

2013

Hsinchu, Taiwan, Republic of China

中華民國一Ｏ二年九月

鎳鍺化物與N型鍺接面摻雜析離對於蕭基位障的影響：使用第一原理計算

研究生：林翰奇　　　　指導教授：崔秉鉞

共同指導教授：林炯源

國立交通大學電子工程學系 電子研究所碩士班

摘要

近年來隨著傳統的矽金氧半場效電晶體技術已經逐漸到達其微縮的極限。為了能夠持續追求元件性能的提升，鍺因為它的載子擁有優越的本質遷移率，被認為在不久的將來可以取代矽作為通道的材料而受到廣泛的研究。然而一般的N型摻雜物例如磷與砷在鍺基板不止固態溶解度比在矽基板還低而且具有更快的擴散速率，所以很難製作出深度很淺的接面。更糟的是，接面的費米能階被釘扎在很靠近鍺價帶的頂端，造成相當高的電子蕭基位障。實驗上發現透過摻雜析離技術可以使得摻雜物在界面析離進而達到更淺的接面深度與更濃的摻雜濃度。但是，摻雜物對於改變界面特性所扮演的角色仍然不是很清楚。

在本篇論文中，我們只用單一的鎳鍺化物（１１２）晶相去簡化真實的多晶鎳鍺化物並與鍺形成接面結構，然後透過第一原理計算使用 LDA 交

換相關能泛函研究N型摻雜物在界面的行為以及使用 HSE06 泛函探討摻雜物析離在界面是否可以有效降低鎳鍺化物與鍺接面的物理蕭基位障。

對於一般的N型摻雜物例如磷與砷而言，我們的計算結果顯示這兩種摻雜物都會在界面析離，雖然磷較偏好析離在界面靠近鎳鍺化物的那一側而砷則是偏好在鍺那一端。這些結果建議我們假若要摻雜磷，在形成鎳鍺化物先植入磷會是個較好的製程選擇；對於摻雜砷，不管製程是在形成鎳鍺化物之前或是之後植入砷，砷都會移到鍺那一端並且堆積在界面。

然後，我們指出這兩種摻雜物析離在界面靠近鍺那一端造成鎳鍺化物與鍺接面的物理蕭基位障降低的量少於 0.1eV，而這麼小的降幅是因為很強的費米能階釘扎效應所造成。順帶一提，當摻雜磷在界面靠近鎳鍺化物的那一側不具有任何降低物理蕭基位障的效果。總結以上的結果，我們認為摻雜析離造成鎳鍺化物與鍺接面特性的改善主要歸功於增加在界面附近的摻雜濃度，少部分是由於物理蕭基位障降低的貢獻。

最後我們探討當摻雜氮這種特殊的情況，計算的結果指出氮可以析離在界面，然而也產生大量的界面態散佈在整個鍺的能隙。雖然鍺的等效導帶邊界透過連續分布的界面態延伸而更接近費米能階，然而界面態在遠離界面約 17 埃即消失殆盡，所以鎳鍺化物與鍺接面的物理蕭基位障還是幾乎

沒有任何改變。

以上這些第一原理的計算結果給予我們更深入的了解對於摻雜物在鎳鍺化物與鍺接面所扮演的角色，也與實驗所觀察到的結果相互呼應。將來，更進一步的計算希望可以協助新製程的開發。

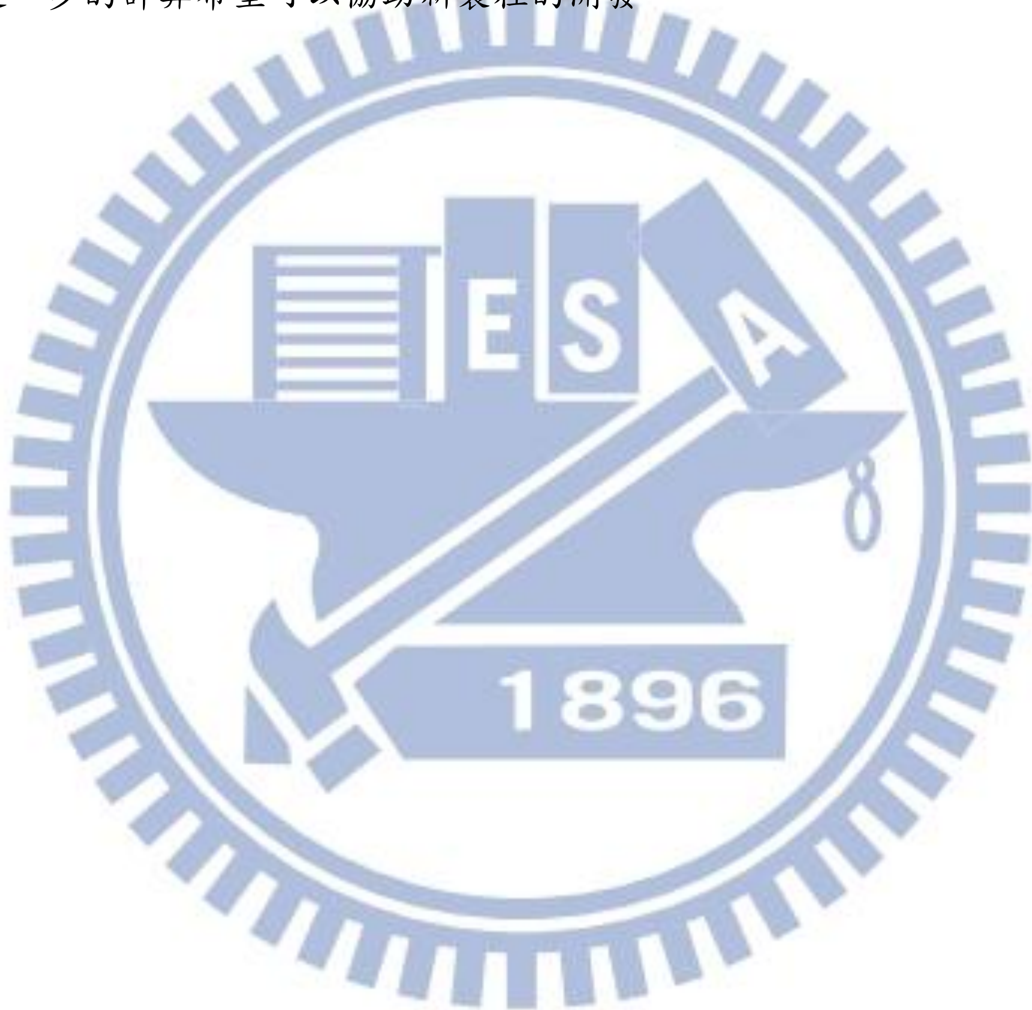

Schottky Barrier Height of the NiGe/n-type Ge Contact with Dopant Segregation: A First-principles Study

Student: Han-Chi Lin Advisor: Bing-Yue Tsui

Co-advisor: Chiung-Yuan Lin

Department of Electronics Engineering

Institute of Electronics

National Chiao Tung University

Abstract

Recently, traditional Si-based MOSFETs are approaching its fundamental scaling limits, and then Ge has been comprehensively explored as a potential channel material to replace Si due to its high intrinsic carrier mobility for further performance enhancement. Nevertheless, the shallow junction depth is hard to form since the conventional n-type dopants such as phosphorous and arsenic have not only lower solid solubility but also faster diffusion rate in Ge substrate than in Si. Moreover, strong Fermi-level pinning near the valence band edge of Ge leads to high electron Schottky barrier height. Dopant segregation technique has been proposed to achieve shallower junction depth and heavier dopant concentration experimentally due to dopant segregated around the interface. However, the role of dopants at the NiGe/Ge interface is not clear.

In this thesis, we build the realistic polycrystalline phases NiGe/Ge contact by including NiGe (112) phase only, and then the first-principles calculations are employed to investigate

the behaviors of the n-type dopant around the interface by LDA functional and whether the physical Schottky barrier height of the NiGe/Ge contact is reduced by dopant segregation or not is calculated by HSE06 hybrid functional.

For the conventional n-type dopant such as phosphorous and arsenic, our calculations show that those two elements may be segregated at the interface, but the preferred segregated site of phosphorous and arsenic are on the NiGe and Ge side, respectively. These results suggest that phosphorous would be a better choice for implantation before germanide process, while arsenic can migrate into the Ge layer and pile up at the interface in both implantation before and after germanide processes.

Then, we show that the physical Schottky barrier height of the NiGe/Ge contact modified by dopant segregation using those two elements on the Ge side is reduced by less than 0.1 eV. This small value is due to the strong Fermi-level pinning effect. By the way, there is no effect to modify the physical Schottky barrier height by doping phosphorous on the NiGe side. To sum up, the improvement of the NiGe/n-type Ge junction characteristics by dopant segregation using phosphorous and arsenic are mainly attributed to the increase of dopant concentration around the interface and partially attributed to the reduction of the physical Schottky barrier height.

For the specific case using nitrogen dopant, the calculated results show that it can be segregated around the interface but yield a large number interface states spreading the Ge bandgap. Although the effective conduction band edge is closer to the Femi level due to continuous interface states, the physical Schottky barrier is almost unchanged since the interface states disappear at about 17 Å away from the interface.

These first-principles calculations provide deep insight on the role of dopants near the

NiGe/Ge interface and can explain the experimental observations very well. Further calculations can also help new process development.

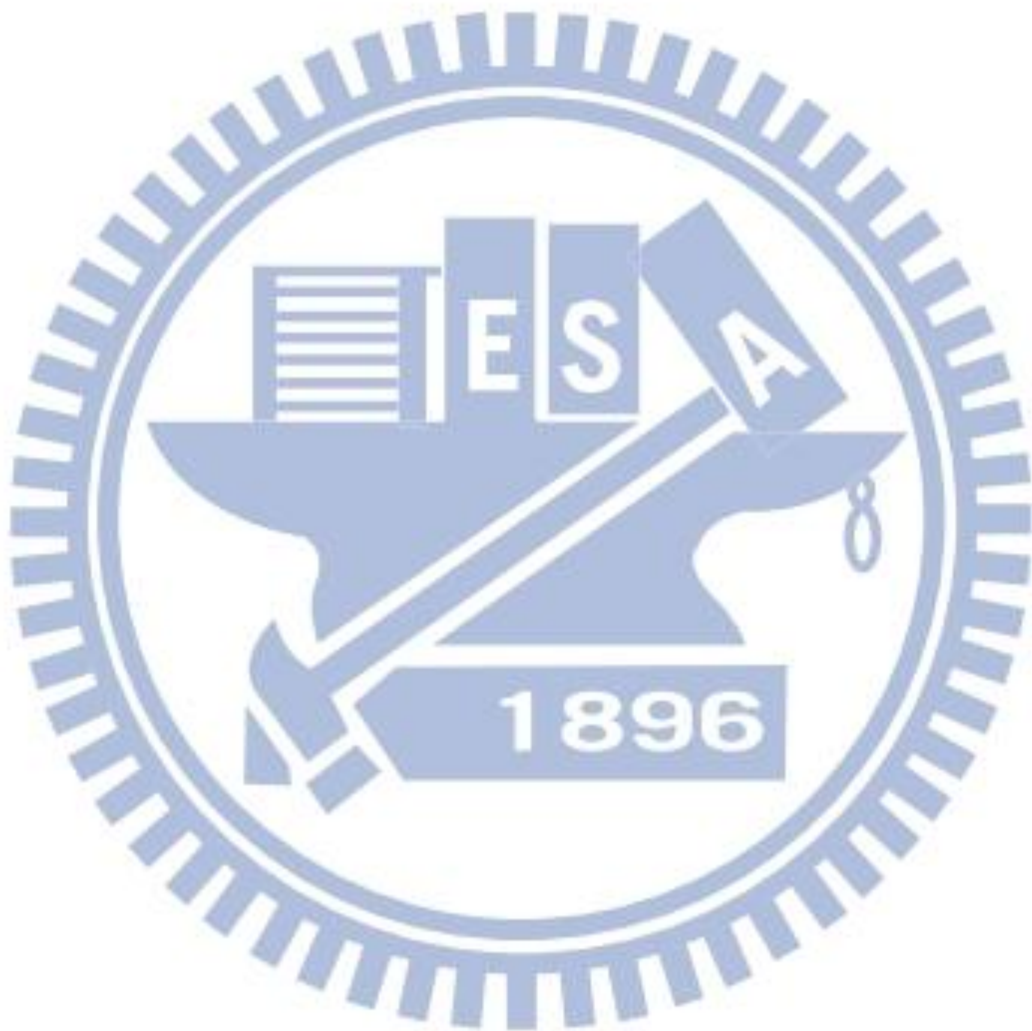

致謝

在攻讀研究所碩士班的這兩年生涯中，首先要感謝指導老師 崔秉鉞博士給予我開啟第一原理計算的鎖匙以及研究的目標，讓我可以用自己感興趣的方法研究我們覺得有意義的主題。對於自己較不熟悉的製程與材料分析上的問題，老師都很有耐心得一一解答我內心的疑問，答案往往也是一針見血。接下來感謝共同指導老師 林炯源博士，從一開始從無到有地教導我理論計算的基礎到中後期當我在研究上遇到計算上的瓶頸時，往往在一天內就可以與老師討論，並且得到很有用且具有彈性的建議順利解決問題。

對於實驗室的大家，首先要感謝已經畢業的振銘學長與子瑜，你們是我進入碩班學習的榜樣，而且不管是專業上還是生活上的困惑都可以與你們討論。謝謝元宏學長、罩哥與嶸健學長，不管問什麼專業上的問題好像都難不倒你們一樣，尤其是有幾次問元宏學長比較微觀的問題，當學長對於自己的答案不是很確定時，都會很有耐心得找書或是查資料，最後告訴我一個正確的答案。而對於一起共患難的滷蛋以及喇叭，能在碩班認識你們，真的沒有什麼遺憾了，謝謝你們，喇叭接下來也要好好加油優!謝謝璽允、泰勞、國丞、雪君有你們陪我談天說地遇到挫折相互鼓勵，也謝謝昕翰、立偉與小弘。

謝謝威智與庭煦學長教我跑第一原理計算的程式，並且根據他們之前的經驗給予我相當適當的建議，幫我減少很多沒有必要的錯誤，尤其謝謝庭煦學長，在我需要跑一些比較久的計算的時候，你總是為我空下 17 的計算資源讓我使用，真的很感謝你。也謝謝昆霖與聖瀚很迅速地幫忙處理工作站的問題，讓我可以無後顧之憂地跑程式!

最後感謝在我背後一直支持我讀完碩班的家人，謝謝爺爺 林智惠先生與阿嬤 林沈素琴 女士，你們省吃儉用就只是為了讓我可以好好專心讀書，真的很謝謝你們的栽培。也謝謝哥哥在我無法陪伴在爺爺奶奶身邊時，照顧他們而且幫我解釋一些他們擔心的事情，讓他們不會這麼擔心，謝謝你!

Contents

Abstract (Chinese) I

Abstract (English) IV

Acknowledgements VII

Contents VIII

List of Tables XI

List of Figures XII

Chapter 1 Introduction 1

1.1 Si-based MOSFETs Scaling Challenges of Source/Drain Design 1

1.1.1 Overview 1

1.1.2 The Impact of the Total On-resistance on MOSFETs Scaling 2

1.2 Properties of Metal/Semiconductor Contacts 3

1.2.1 Schottky Barrier Height 3

1.2.2 Fermi-level Pinning 3

1.2.3 Specific Contact Resistance 4

1.3 Modified Schottky Barrier (MSB) Height Method 5

1.4 Pros and Cons of Germanium 6

1.5 Motivation 8

1.6 Organization 10

Chapter 2 Calculation Methods 16

2.1 Representational Approaches before Density Functional Theory 16

2.1.1 The Born-Oppenheimer approximation... 17

2.1.2 The Hartree-Fock approximation 18

2.2 Density Functional Theory (DFT) 21

2.2.1 The Hohenberg-Kohn Theorem.. 22

2.2.2 The Kohn-Sham Formulation... 24

2.3 The Exchange-correlation functional 27

2.3.1 The local density approximation (LDA) 27

2.3.2 The generalized gradient approximation (GGA).................................... 29

2.3.3 Hybrid functionals 31

Chapter 3 Results and Discussion 34

3.1 Choosing Exchange-correlation Functional 34

3.2 Structural Modeling of the NiGe/Ge Contact.. 35

3.2.1 Behaviors of Segregated Dopant around the Interface 37

3.2.2 Barrier Height Modified by Dopant Segregation 38

3.3 Effect of Nitrogen Dopant Segregated on the NiGe/Ge Contact....................... 40

Chapter 4 Conclusion and Future works 61

4.1 Conclusions 61

4.2 Future Works 63

References 64

Author's Biography 68

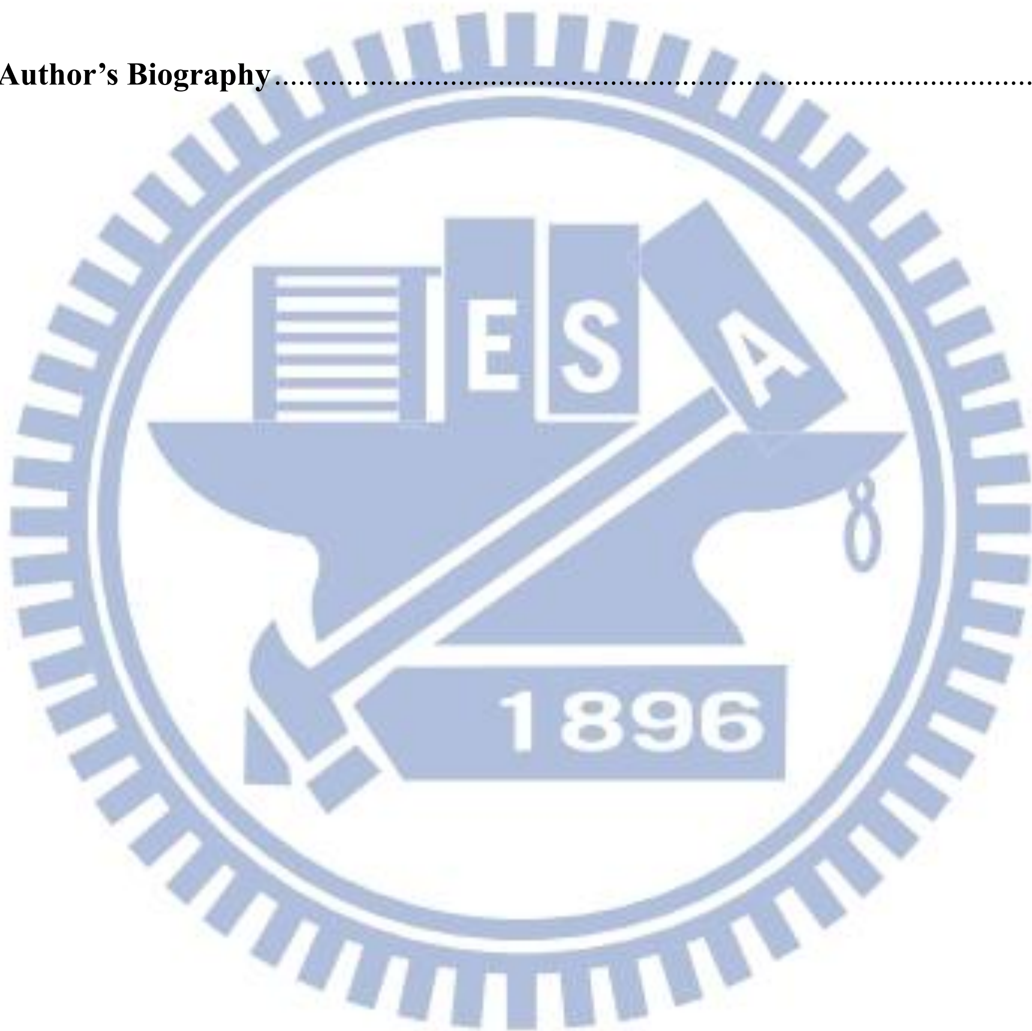

List of Tables

Chapter 1

Table 1-1 Material characteristics of alternative channel materials [10]. 11

Chapter 3

Table 3-1 Calculated lattice constant (second row) and also the Ge-bulk bandgap (fourth to eighth rows) at the various lattice constant using different exchange-correlation functionals. The experimental lattice constant and bandgap are 5.658 Å and 0.785 eV [42], respectively. 43

Table 3-2 Specific lateral surface vectors chosen for the NiGe(112)/Ge(001) interface strucutre. 44

Table 3-3 Specific lateral surface vectors chosen for the NiGe(210)/Ge(001) interface strucutre. 44

Table 3-4 Specific lateral surface vectors chosen for the NiGe(111)/Ge(001) interface strucutre. 45

Table 3-5 Total energy of the various choices of lateral matching with NiGe(112)T4 and Ge(001) slabs. 45

Table 3-6 Total energy of the various choices of lateral matching with NiGe(112)T8 and Ge(001) slabs. 46

List of Figures

Chapter 1

Figure 1-1 Number of transistors on the CPU has been increased from 1971 to 2011; the line corresponds to exponential growth with Moore's law. (source: Wikipedia)...... 12

Figure 1-2 N-type Metal-Oxide-Semiconductor Field-Effect-Transistor (nMOSFET) device simulation showing series and strained Si channel resistances becoming equivalent at approximately the 32 nm logic node [2]...................................... 12

Figure 1-3 Schematic representation of source/drain structure and series resistance components [3].. 13

Figure 1-4 Relative contribution from each component of the resistance to series resistance for different technology nodes [4]... 13

Figure 1-5 Schematic band diagram of band bending according to the Schottky-Mott model of the metal/n-type semiconductor: (a) Before contact and (b) after contact formation [26]. 14

Figure 1-6 Schematic band diagram of band bending according to the Bardeen model of the metal/n-type semiconductor: (a) Before contact and (b) after contact formation. The Fermi-level is pinned by the high density of surface states at the semiconductor interface [26].. 14

Figure 1-7 Conduction mechanics for metal/semiconductor contacts, (a) thermionic emission (b) thermionic-field emission (c) field emission................................ 15

Figure 1-8 Sub-100 nm transistor technology scaling. (source: Intel Corp.)....................... 15

Chapter 3

Figure 3-1 Conventional cell of the Ge bulk. 47

Figure 3-2 Atomic structure of the NiGe bulk. 47

Figure 3-3 Calculated band structure of the Ge bulk by HSE06. The red crosses stand for the high-symmetry points as measured by thr photoemission experiments. The enerygy reference is set at the Fermi-level. 48

Figure 3-4 Process flow of the self-aligned NiGe n^+/p junction. 48

Figure 3-5 X-ray diffraction (XRD) sprectrum of the NiGe/Ge structure formed by 350°C annealing shows polycrystalline NiGe phases. 49

Figure 3-6 Lateral cell shape of the NiGe(112), (210), and (111) slabs on the Ge(001) surface. 49

Figure 3-7 One of the surface terminations of the NiGe(112) slab, called NiGe(112)T4 slab, contains 4 atoms (2 Ni and 2 Ge atoms) per lateral unit cell. 50

Figure 3-8 One of the surface terminations of the NiGe(112) slab, called NiGe(112)T8 slab, contains 8 atoms (4 Ni and 4 Ge atoms) per lateral unit cell. 50

Figure 3-9 Various choices of lateral matching of the NiGe(112) and Ge(001) slab. The a and b stand for the origin offset of the NiGe slab at x and y direction, respectively. 51

Figure 3-10 Atomic structure of the NiGe/Ge contact. 51

Figure 3-11 Total energy of the NiGe/Ge interface structure with one Ge atom being substituted for a phosphorous, where the energy reference is taken to be the

cases with the most left substitutional sites. 52

Figure 3-12 Total energy of the NiGe/Ge interface structure with one Ge atom being substituted for an arsenic, where the energy reference is taken to be the cases with the most left substitutional sites. 52

Figure 3-13 Secondary ion mass spetroscopic (SIMS) profiles shows the phosphorous segregation at the NiGe/Ge(001) interface with a NiGe thickness of 60 nm [23]. 53

Figure 3-14 Secondary ion mass spetroscopic (SIMS) profiles shows the arsenic segregation at the NiGe/Ge(001) interface with a NiGe thickness of 60 nm [23]. 53

Figure 3-15 Bandgap of the Ge(001) slab as a function of the nuber of atomic layers. 54

Figure 3-16 Partial density of states (PDOS) of the Ge atom in the pure 16-layers Ge(001) slab. 54

Figure 3-17 Partial density of states (PDOS) of the Ge atom labeled as SG9b (see Figure 3-10) in the undoped NiGe/Ge interfacial structure. 55

Figure 3-18 Partial density of states (PDOS) of the Ge atom labeled as SG9b (see Figure 3-10) in the NiGe/Ge interface structure when doping phosphorous at the most stable position. 55

Figure 3-19 Partial density of states (PDOS) of the Ge atom labeled as SG9b (see Figure 3-10) in the NiGe/Ge interface structure when doping phosphorous at the metastable site. 56

Figure 3-20 Partial density of states (PDOS) of the Ge atom labeled as SG9b (see Figure

3-10) in the NiGe/Ge interface structure when doping arsenic at the most stable position. 56

Figure 3-21 Current-voltage characteristics of the NiGe/Ge junction without and with phosphorous segregation [44]. 57

Figure 3-22 Current-voltage characteristics of the NiGe/Ge junction without and with arsenic segregation [44]. 57

Figure 3-23 Partial density of states (PDOS) of the Ge atom labeled as SG9b (see Figure 3-10) in the NiGe/Ge interface structure when doping nitrogen at the most stable position. 58

Figure 3-24 Partial density of states (PDOS) of the Ge atom labeled as SG1b (see Figure 3-10) in the NiGe/Ge interface structure when doping nitrogen at the most stable position. 58

Figure 3-25 Partial density of states (PDOS) of the Ge atom labeled as SG5b (see Figure 3-10) in the NiGe/Ge interface structure when doping nitrogen at the most stable position. 59

Figure 3-26 Partial density of states (PDOS) of the Ge atom labeled as SG13b (see Figure 3-10) in the NiGe/Ge interface structure when doping nitrogen at the most stable position. 59

Figure 3-27 Bandgap of the Ge atom in the NiGe/Ge interface structure when doping nitrogen at the most stable position as a function of the distance far from the interface. The gray lines stand for the interface states spreading the Ge bandgap. 60

Chapter 1
Introduction

1.1 Si-based MOSFETs Scaling Challenges of Source/Drain Design

1.1.1 Overview

The integrated circuits (ICs) industry has been growing rapidly, benefiting from the dimension scaling of Si-based metal-oxide-semiconductor field-effect-transistors (MOSFETs) for more than half a century. Since then, more and more transistors are able to be integrated into a single chip as shown in Figure 1-1. Moore's law is named after Gordon E. Moore who projected firstly the number of transistors on ICs doubles approximately every two years in 1965 [1]. The scaling not only decreases production cost per transistor and power consumption but also increases the circuit density and device speed.

A successful device design tends to enhance the on-current at the allowable off-state leakage for the performance requirements during scaling. However, several negative short-channel effects would arise from device scale-down. As the gate length of MOSFETs are reduced, the channel potential influenced by the source/drain increases relative to the gate. Escalating off-state leakage arises from threshold voltage roll-off and drain-induced barrier lowering (DIBL), which describe smaller threshold voltage at shorter gate length and higher drain voltage, may hinder transistor scaling because of significant passive power consumption. In order to reduce the source and drain influence on the channel potential in bulk device, the ultra-shallow junction formation technologies are necessary to minimize these short-channel effects.

1.1.2 The Impact of the Total On-resistance on MOSFETs Scaling

The total on-resistance of the MOSFETs is the summation of channel resistance and series resistance. The channel resistance diminishes aggressively with the scaling of the gate length and the carrier mobility enhancement by uniaxial stain technology, while the series resistance is difficult to be reduced due to the decrease of contact area and junction depth. Unfortunately, escalating series resistance might limit the device on-current for performance enhancement. Figure 1-2 shows the simulated channel resistance and series resistance of NMOSFET at various technology nodes. It demonstrates the increasing trend of series resistance, converse to the trend of decreasing channel resistance with transistor scaling. It is observed that the series resistance would be comparable to the channel resistance at the 32-nm logic node [2]. Therefore, reduction of series resistance represents one of the fateful challenges for continued aggressive scaling.

The series resistance can be divided into four components: source/drain extension (SDE) to gate overlap resistance (R_{ov}); SDE resistance (R_{ext}); deep source/drain resistance (R_{dp}); and silicide-diffusion contact resistance (R_{csd}) as shown in Figure 1-3 [3]. To successfully optimize the source/drain design for lower series resistance, it is important to understand the relative contribution of each component. Among these components, the R_{csd} and R_{ov} are the dominant components and account for more than 80% of the total series resistance at all technology nodes as shown in Figure 1-4 [4]. It is noted that the contribution of R_{csd} escalates as the transistor scaling, while R_{ov} is almost at the same level. As a result, the R_{csd} is the most serious component to be reduced.

1.2 Properties of Metal/Semiconductor Contacts

1.2.1 Schottky Barrier Height

For reduction of contact resistance, the characterizations of metal/semiconductor should be prior to understanding. The rectifying properties of the metal/semiconductor contacts discovered by Ferdinand Braun in 1874 are determined by the barrier height of the majority carrier using the simple model proposed independently by Schottky and Mott [5]. The barrier height equals the energy difference between the Fermi level and the edge of the respective majority carrier band, i.e., the conduction-band minimum for n-type semiconductors or the valence-band maximum for p-type semiconductors [6].

In the case that an n-type semiconductor and a metal with higher work function come in electric contact, the two Fermi levels are forced to coincide and electrons pass from the semiconductor into metal. The excess of negative charge on the metal surface and the positive space-charge in the depletion layer near the semiconductor surface form an interface dipole and result in band bending regime as shown in Figure 1-5. The n-type Schottky barrier height (SBH) calculated by the Schottky-Mott model is given by:

$$\phi_B = \phi_M - \chi,$$

where ϕ_B is the barrier height, ϕ_M is the metal work function, and χ is the electron affinity, which describes the energy difference between the bottom of the conduction band and the vacuum level at the semiconductor surface.

1.2.2 Fermi-level Pinning

The above equation shows that the barrier height depends linearly on the metal work function and demonstrates by the experimental results of ionically bonded semiconductors [6].

However, some covalently bonded semiconductors such as Si, Ge, and GaAs do not confirm this relationship because the barrier height depends weakly on the metal work function. In 1947, Bardeen proposed the different model to explain the insensitivity of the Schottky barrier height to the metal work function as shown in Figure 1-6 [7]. It is shown that if the high density of localized interface states at the semiconductor interface distribute in the semiconductor energy bandgap, those interface states would absorb most of the majority carriers on the semiconductor side. Consequently, different excess charge density on the metal side will cause only slight variations of the space-charge density. As a result, the barrier height will become almost independent of the metal work function. Such behavior is called Fermi-level pinning (FLP).

1.2.3 Specific Contact Resistance

In order to simply compare values of contact resistance with different contact size (A_c), an appropriate parameter named specific contact resistance (ρ_c), which is independent of contact size, is introduced and defined as the reciprocal of the derivative of current density (J) to the voltage (V) at zero bias, as shown in the following expression:

$$\rho_c \equiv \left(\frac{\partial J}{\partial V}\right)^{-1}_{V=0} = R_c \cdot A_c,$$

where Rc is the contact resistance and Ac is the contact area.

The current-voltage relations based on thermionic emission (TE), thermionic-field emission (TFE), and field emission (FE) with different doping level in contact region as shown in Figure 1-7 have been derived from a doping dependent tunneling probability using Wentzel-Kramers-Brillouin (WKB) approximation [8].

Thermionic emission (TE) is the carrier transport over the barrier by thermal excitation

only due to wide depletion width from the metal/semiconductor lightly doped contact region, therefore, primarily relating to the built-in barrier height. The corresponding specific contact resistance is derived as:

$$\rho_c(TE) = \left(\frac{k}{qA_c}\right) T \cdot exp\left(\frac{q\phi_B}{kT}\right),$$

where k is the Boltzmann constant and T is the absolute temperature.

For contact region with heavy doping concentration, the carrier could directly tunnel through the whole barrier since the depletion layer is sufficiently narrow. In this case, field emission (FE) process dominates the current density, thus specific contact resistance is given by:

$$\rho_c(FE) \propto exp\left[\frac{2\sqrt{\varepsilon_s m^*}}{\hbar}\left(\frac{\phi_B}{\sqrt{N_d}}\right)\right],$$

where ε_s is the permittivity of the semiconductor, m^* is the tunneling effective mass, $\hbar$ is the reduced Planck constant, and N_d is the active dopant concentration.

In addition, thermionic-field emission (TFE) dominates when the depletion region is reduced enough to allow some tunneling through the barrier for the medium level of doping contact region. To sum up, the theory predicts that reduction of specific contact resistance could be achieved by decreasing the barrier height and/or increasing the active doping concentration N_d near the metal/semiconductor interface.

1.3 Modified Schottky Barrier (MSB) Height Method

Increasing doping concentration for strong band bending near contact interface and/or decreasing the physics Schottky barrier height could reduce the contact resistance. Hence,

implant-to-silicide and/or dopant segregation technique are introduced for the above-mentioned reasons. Implant-to-silicide is the technique that silicide formation is prior to dopant implantation, then the implanted dopant could diffuse out from silicide by annealing at low temperature and segregate at the interface due to different diffusion coefficient between silicide and silicon substrate. On the other hand, dopant segregation is the process that dopant implanted before silicide formation. If silicidation is performed on the doped silicon regions, the dopants could be redistributed and segregated at the interface as a result of the different solid solubility of dopant in silicide and silicon substrate. Therefore, high doping concentration as a result of the pile-up of the segregated dopant at the interface could cause strong band bending to reduce the effective Schottky barrier height. The metal/semiconductor Schottky contact with high barrier height could be changed to Ohmic contact.

1.4 Pros and Cons of Germanium

As Si-based transistor reaches sub-100 nm technology nodes, the conventional device scaling cannot continue to maintain the required performance. Thus, the SiGe source/drain was introduced to achieve uniaxial strain in the channel to enhance electron mobility at 90 nm node [9]. However, the strain technology is approaching its limits as a performance booster beyond 22 nm node. Once the traditional performance enhancement slows down, alternative high-carrier-mobility materials such as germanium (Ge) and Ⅲ - V compound semiconductors are considered as potential candidates to replace Si in the channel for further performance enhancement as shown in Figure 1-8 [10].

The characteristics of several potential channel materials at 300 K are listed in Table 1-1 [10]. Bulk hole mobility of Ge is the highest among all of the known semiconductor and bulk electron mobility of Ge is approximately two times higher than Si. By just looking at the

mobility values, the best combination seems to be Ge for PMOS and Ⅲ-Ⅴ compound semiconductor for NMOS. However, it is easier to fabricate transistors in Ge than Ⅲ-Ⅴ compound semiconductor due to its good compatibility with conventional Si process such as self-aligned low-resistivity metal germanide formation at low thermal budget. Another advantage for Ge is much larger on-current achieved as a result of larger density of states (DOS) in the conduction band than Ⅲ-Ⅴ compound materials. There are severe technical issue of surface passivation in Ⅲ-Ⅴ compound semiconductor. Moreover, the availability of high-k dielectrics compensates for the lack of a stable Ge-oxide in the past. Consequently, the pure Ge channel is a promising solution for high performance logic CMOS scaling.

Nevertheless, Ge has a smaller bandgap than Si substrate as shown in Table 1-1. It would result in higher junction leakage. This also implies that the quality of source/drain junction will play an important role in the device performance. Ultra-shallow p^+/n junction can be achieved by a pre-amorphization implant (PAI) before boron ion implantation. The implanted boron almost much less diffuses at 400˚C ~ 600˚C temperature range required for dopant activation in Ge [11]. Numbers of researches about Ge p-MOSFETs have been published and indicated its potential for a replacement for traditional Si-based [12].

However, the n-type dopants such as phosphorous and arsenic have lower activation level by conventional annealing due to their low solid solubility [13]. They also have faster diffusion rate in Ge substrate than in Si [14-18]. It would drastically reduce the Ge n-MOSFETs performance since low contact resistance and shallow junction depth are hard to be achieve. Moreover, strong Fermi-level pinning (FLP) at the valence band edge of Ge due to metal-induced gap states (MIGS) at metal/Ge interface causes Ohmic and Schottky characteristics to metal/p-Ge and metal/n-Ge junctions, respectively. As mentioned above,

high electron Schottky barrier height of about 0.5~0.6 eV is very difficult to form low resistance metal/n-Ge contact. Thus, how to accomplish Ohmic contact and ultra-shallow n+/p Ge junction are critical challenges.

1.5 Motivation

As Si-based MOSFETs are approaching its scaling limit, many advanced materials and architectures are proposed for further performance enhancements. Ge is an attractive channel material to enhance the performance of MOSFETs as a result of its high carrier mobility. However, high performance n-channel Ge MOSFETs still suffer from many difficulties to be solve, especially for the issue of high source/drain contact resistance and the formation of ultra-shallow junction due to strong Fermi-level pinning near the Ge valence band edge, poor activation efficiency by conventional annealing, and high diffusion rate of n-type dopant such as phosphorous and arsenic in Ge.

The techniques such as implant to silicide and dopant segregation have been proved to reduce the effective Schottky barrier height of metal silicide/Si contacts due to the increase of the dopant concentration at the silicide/Si interface [19-22]. The effect of those modified Schottky barrier methods on the metal germanide/n-Ge contacts is needed to be examined carefully since the Fermi-level pinning on Ge is stronger than Si system, but very few works explored it in depth. The effective Schottky barrier height of the NiGe/n-Ge contact by dopant segregation lowering from 0.72 eV at 0 K to 0.38 eV using phosphorous and to 0.19 eV using arsenic has been reported in [23]. However, traditional Schottky barrier height extraction from the measured I-V characteristics only considers thermionic emission model and would lead to underestimation of the barrier height since field emission, which is the dominate machine of current transport, is not included in the extraction methods. Therefore, the very low effective

Schottky barrier height extracted only including thermionic emission is not necessarily true.

On the other hand, Second Ion Mass Spectrometry (SIMS) is regarded as a reliable technique to obtain accurate dopant depth profiles of the source/drain contact with respect to junction depth, implanted dose and profile shape. However, the dopant profile especially in the regions less than 20 nm below the surface might be affected by conditions such as the transient region that exists until sputtering becomes stable, the sputter rate changing near the interface as a result of the different materials being crossed, and ion beam-induced interlayer mixing since atoms from outer atomic layer can be driven into deeper layer during analysis [24]. According to the International Technology Roadmap for Semiconductors (ITRS), the ultra-shallow junction depth of the source/drain extension is required to be around 10 nm at the 22 nm technology node [25]. Therefore, many analysis conditions should be carefully considered to provide precise dopant depth profiles of the ultra-shallow junction beyond 22 nm logic node.

As mention previously, modeling and understanding the modified Schottky barrier height through dopant segregation for the ultra-shallow junction are challenged by accurate dopant profiling using SIMS analysis and precise barrier height extraction. The *ab-initio* density functional theory (DFT) calculation is appropriate for addressing these challenges from first-principles. These calculations from first-principles provide the physical properties of a given system just from the knowledge of the element and position of the atoms. Judging from the difficulty in lowering high electron Schottky barrier height for NiGe/n-Ge contact and dopant segregation as an appropriate formation technique for ultra-shallow junction, a first-principles calculation can be employed to reveal how stable atomic structures with different segregated doping elements such as phosphorous and arsenic are, and understand

whether the segregated doping atoms affect the physical Schottky barrier height or not.

1.6 Organization

In this thesis, the first chapter is the introduction consisting of the Si-based MOSFETs scaling challenges focusing on source/drain improvement mainly, the merits and drawbacks of Ge which is regarded as a potential material to replace Si, the problems for underestimation of barrier height using traditional extraction methods in the low barrier system, and finally proposing a first-principles calculations to overcome these problems and to understand the influence of dopant segregation on the NiGe/n-type Ge contact.

Chapter 2 shows some representational approximations for many-body problems before density functional theory, the frameworks of the density functional theory including the Hohenberg-Kohn theorem and Kohn-Sham formulation, and the introduction of the exchange-correlation energy functional used in the our calculations.

Simulation result is shown and discussed in Chapter 3. First, we examine the result of lattice constant and band structure for Ge bulk to find the suitable exchange-correlation functional. Then, the atomic structure of the NiGe/Ge contact consisting with the experimental simple is constructed. Finally, the behaviors of the conventional n-type dopant around the interface, the effect of the Schottky barrier height modified by dopant segregation, and the influence of the nitrogen dopant segregated at the interface are studied by the first-principles calculations. The last chapter is the conclusions and future works of this thesis.

Table 1-1 Material characteristics of alternative channel materials [10].

	Si	Ge	GaAs	InSb
Bandgap, E_g (eV)	1.12	0.66	1.42	0.17
Hole mobility, μ_h ($cm^2V^{-1}s^{-1}$)	450	1900	400	1250
Electron mobility, μ_e ($cm^2V^{-1}s^{-1}$)	1500	3900	8500	80000
Effective density of states in valence band, N_V (cm^{-3})	1.04×10^{19}	6.0×10^{18}	7.0×10^{18}	7.3×10^{18}
Effective density of states in conduction band, N_C (cm^{-3})	2.8×10^{19}	1.04×10^{19}	4.7×10^{17}	4.2×10^{16}

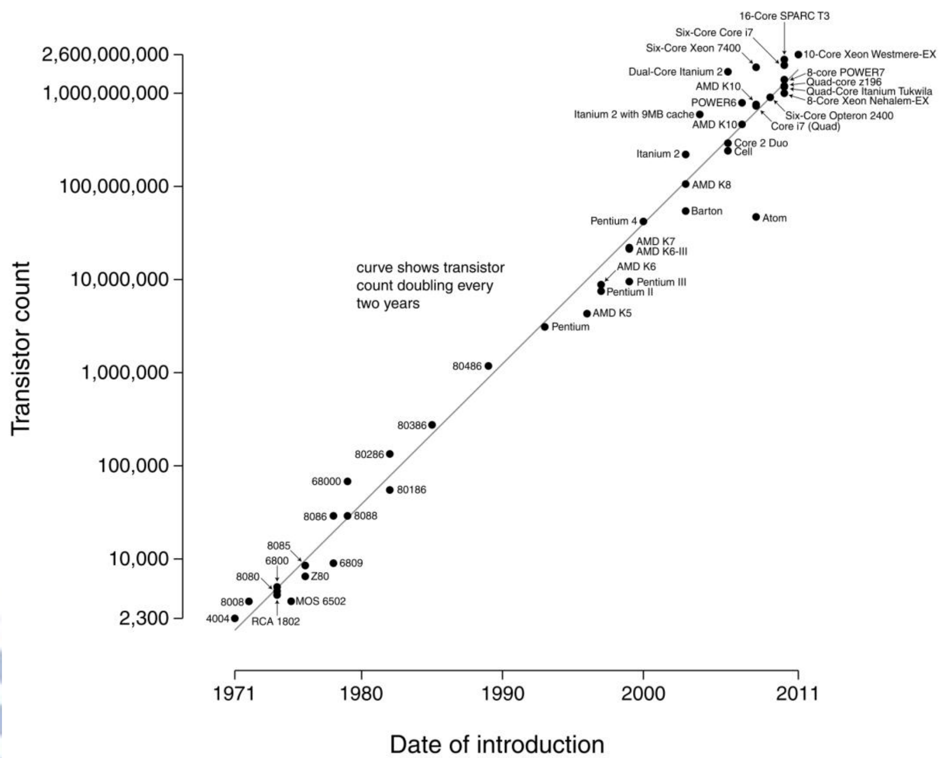

Figure 1-1 Number of transistors on the CPU has been increased from 1971 to 2011; the line corresponds to exponential growth with Moore's law. (source: Wikipedia)

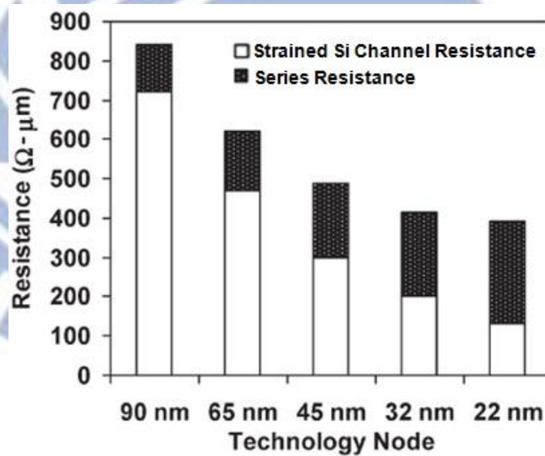

Figure 1-2 N-type Metal-Oxide-Semiconductor Field-Effect-Transistor (n-MOSFET) device simulation showing series and strained Si channel resistances becoming equivalent at approximately the 32 nm logic node [2].

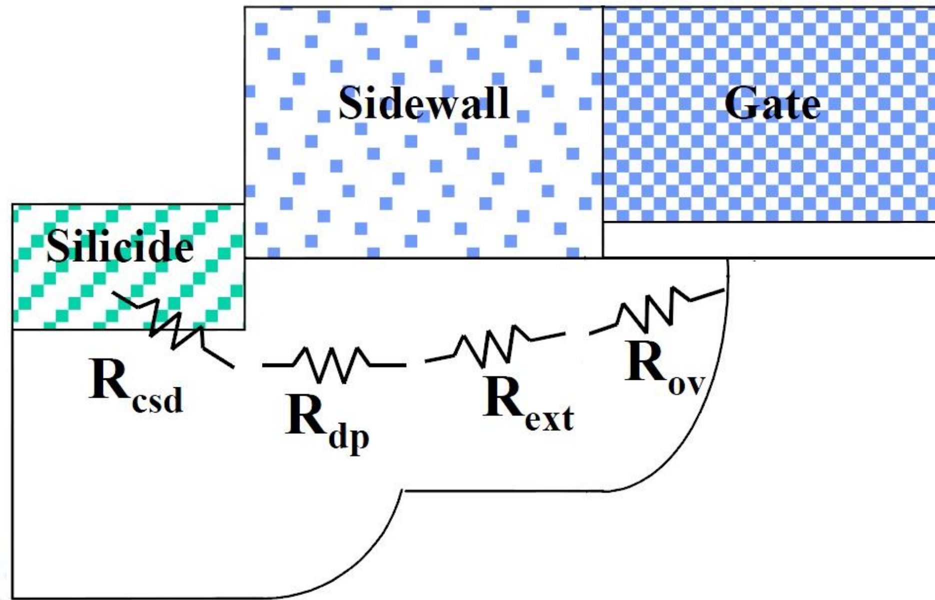

Figure 1-3 Schematic representation of source/drain structure and series resistance components [3].

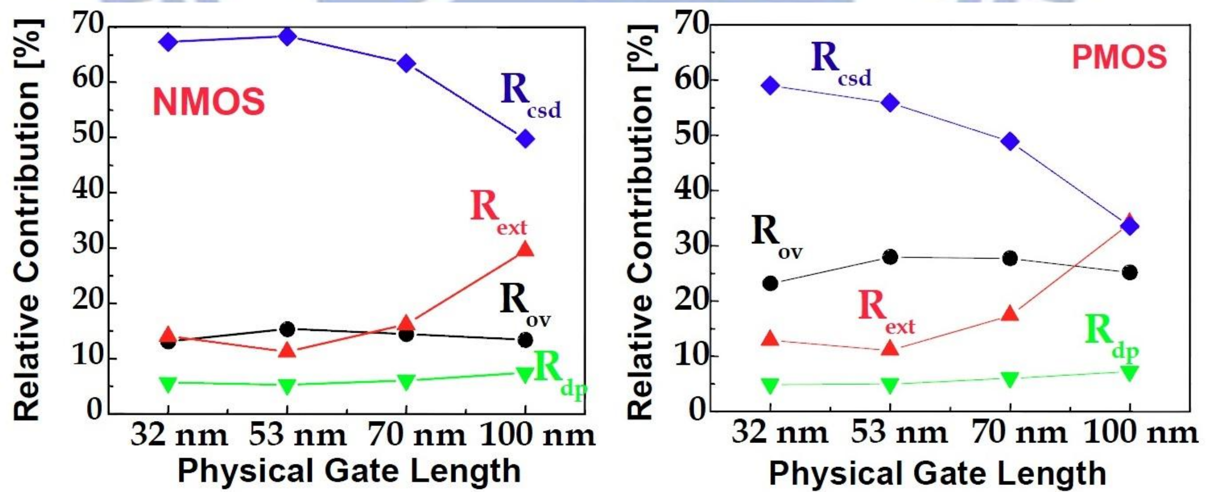

Figure 1-4 Relative contribution from each component of the resistance to series resistance for different technology nodes [4].

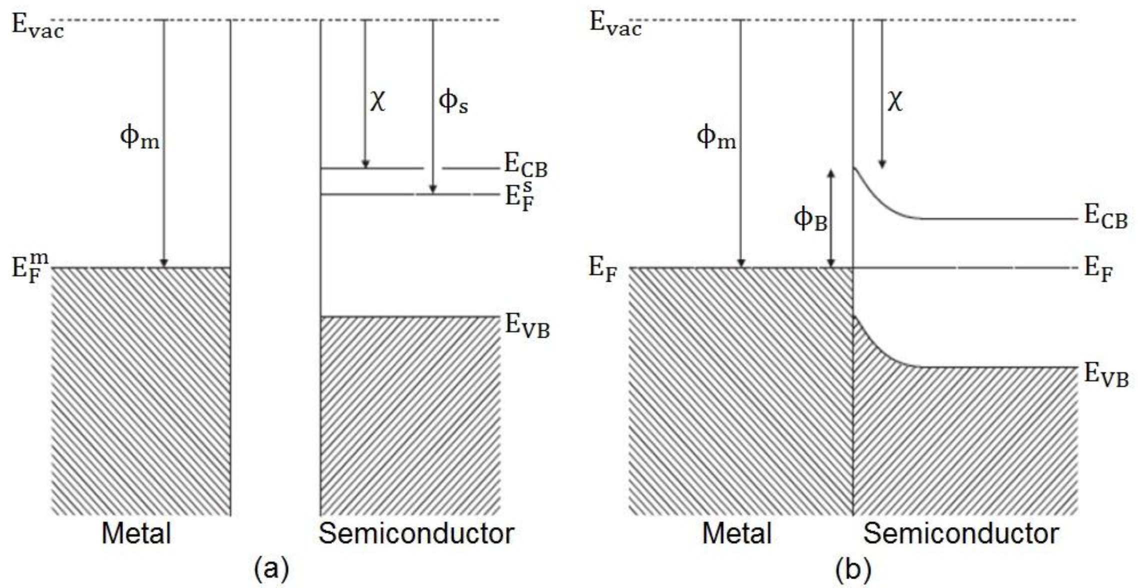

Figure 1-5 Schematic band diagram of band bending according to the Schottky-Mott model of the metal/n-type semiconductor: (a) Before contact and (b) after contact formation [26].

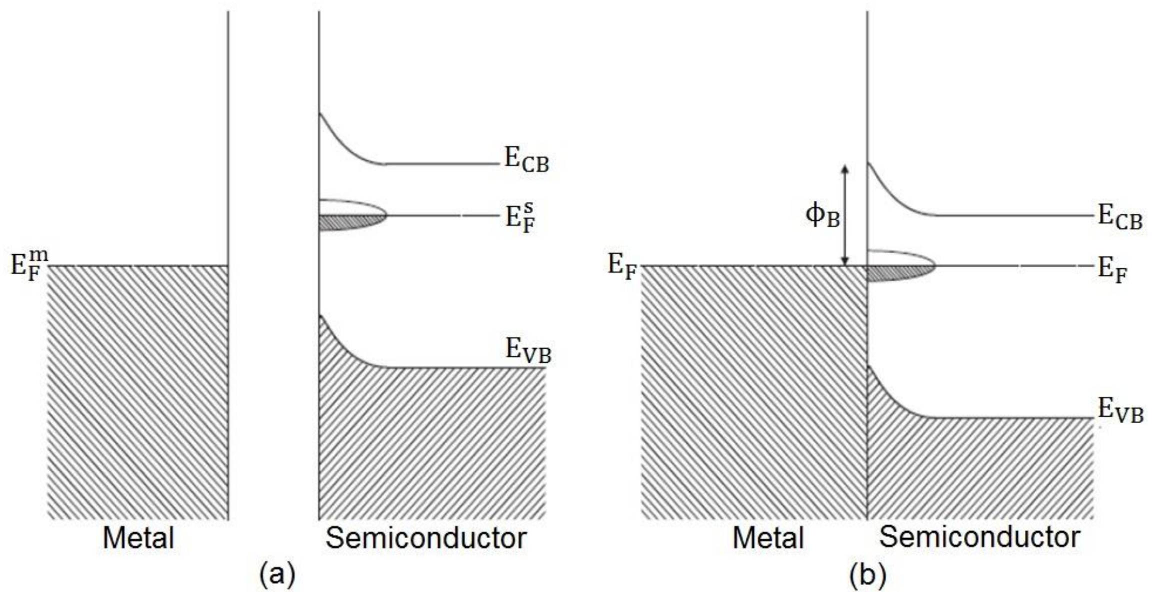

Figure 1-6 Schematic band diagram of band bending according to the Bardeen model of the metal/n-type semiconductor: (a) before contact and (b) after contact formation. The Fermi-level is pinned by the high density of surface states at the semiconductor interface [26].

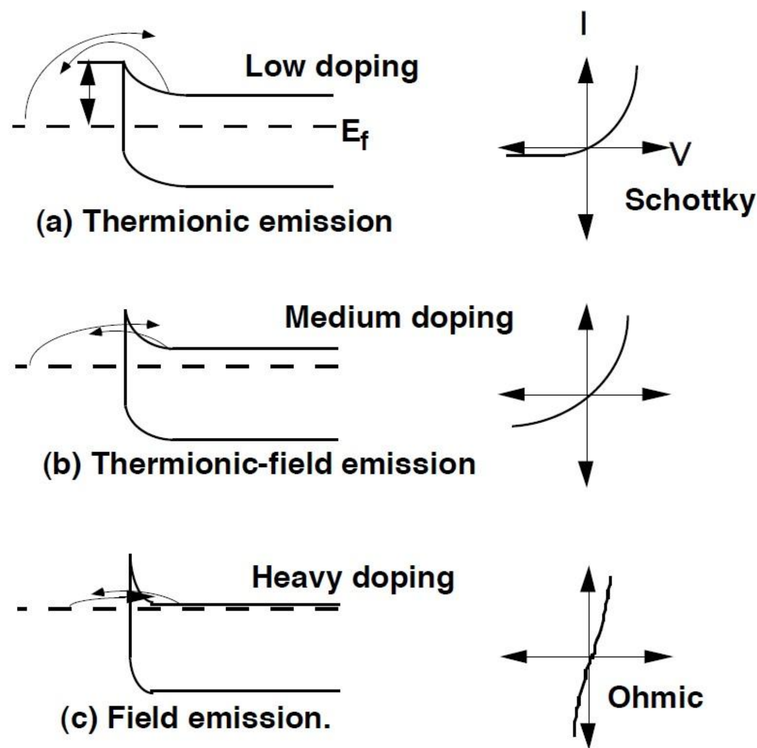

Figure 1-7 Conduction mechanics for metal/semiconductor contacts, (a) thermionic emission (b) thermionic-field emission (c) field emission.

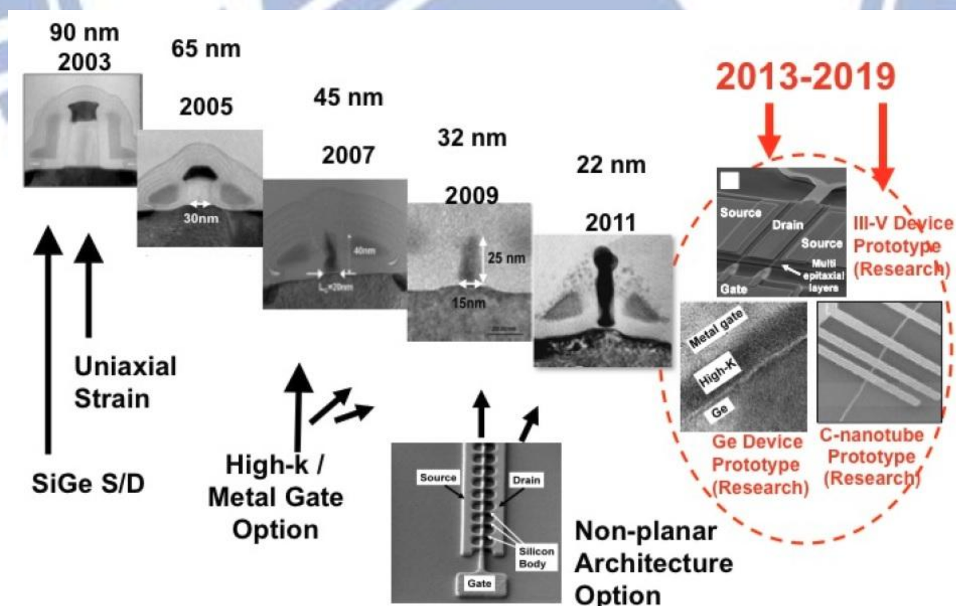

Figure 1-8 Sub-100 nm transistor technology scaling. (Source: Intel Corp.)

Chapter 2

Calculation Methods

2.1 Representational Approaches before Density Functional Theory

For the many-body system consisted of N electrons (of coordinates $\boldsymbol{r}$, mass m, and charge $-e$) and corresponding nuclei (of coordinates $\boldsymbol{R}$, mass M_I, and charge $+Z_I e$), electrons in material are subjected both to electron-electron interactions and to external potentials in the real world. The starting point for the theoretical description of many-body system is the nonrelativistic, time-independent Hamiltonian of the coupled electron-nucleus system

$$\hat{H}_{tot}(\boldsymbol{r},\boldsymbol{R}) = \hat{T}_n(\boldsymbol{R}) + \hat{T}_e(\boldsymbol{r}) + \hat{V}_{en}(\boldsymbol{r},\boldsymbol{R}) + \hat{V}_{nn}(\boldsymbol{R}) + \hat{V}_{ee}(\boldsymbol{r})$$

$$= -\frac{\hbar^2}{2M_I}\sum_I \nabla_I^2 - \frac{\hbar^2}{2m}\sum_{i=1}^{N}\nabla_i^2 - \sum_{i,I}\frac{Z_I e^2}{|\boldsymbol{r}_i-\boldsymbol{R}_I|} + \frac{1}{2}\sum_{I\neq J}\frac{Z_I Z_J e^2}{|\boldsymbol{R}_I-\boldsymbol{R}_J|} + \frac{1}{2}\sum_{i\neq j}\frac{e^2}{|\boldsymbol{r}_i-\boldsymbol{r}_j|}, \quad (2.1)$$

where $\hat{T}_n$ is the kinetic energy of the nuclei, $\hat{T}_e$ is the kinetic energy of the electrons, $\hat{V}_{en}$ is the electron-nucleus attraction, $\hat{V}_{nn}$ is the nucleus-nucleus repulsion, and $\hat{V}_{ee}$ is the electron-electron repulsion, respectively.

In principle, all the properties of such system can be described by the many-body wavefunction $\Psi(\boldsymbol{r},\boldsymbol{R})$, which is the solution of the many-body stationary Schrödinger equation

$$\hat{H}_{tot}\Psi(\boldsymbol{r},\boldsymbol{R}) = E\Psi(\boldsymbol{r},\boldsymbol{R}). \quad (2.2)$$

Once the wavefunction is solved, any observable $\langle\hat{O}\rangle$ can be determined by the expectation value of the corresponding operator

$$\langle\hat{O}\rangle = \frac{\langle\Psi(r,R)|\hat{O}|\Psi(r,R)\rangle}{\langle\Psi(r,R)|\Psi(r,R)\rangle}. \quad (2.3)$$

Careful use of symmetry might help us reduce the size of the Hamiltonian, and the escalating power of modern computers growing exponentially with time allow us to consider larger system, but it is still difficult to solve exact numerical diagonalization for the problem of N electrons interacting in some external potential since the size of the Hilbert space of our N-electron problem grows much faster than exponentially with N. Therefore, proper approximations and simplifications are needed to extract useful information from such complex systems.

2.1.1 The Born-Oppenheimer approximation

The adiabatic approximation, first proposed by Born and Oppenheimer is based on the fact that the typical velocity of an electron in materials is much faster than the velocity of the nucleus, since the nuclear mass is about one thousand times heavier than electronic mass in realistic situations [27]. In other words, the time scale of the nuclear motion is several orders of magnitude larger than that of the electronic motion. Therefore, it can be assumed that at any moment the electrons will be in their instantaneous ground state determined by the interaction with nuclear distribution at a particular instant, and then the forces acting on the nuclei are determined by the instantaneous electronic distribution and the nuclear positions of the system. Based on such an assumption, the nuclear kinetic energy is considered to be negligible, and the nuclear positions are taken as fixed external parameters.

As a result, the Hamiltonian for the coupled electron-nucleus system can be reduced to the Hamiltonian for the N interacting electrons in an external potential

$$\begin{aligned}\hat{H} &= \hat{T}_e + \hat{V}_{ee} + \hat{V}_{ext} \\ &= -\frac{\hbar^2}{2m}\sum_{i=1}^{N}\nabla_i^2 + \frac{1}{2}\sum_{i\neq j}\frac{e^2}{|\boldsymbol{r}_i-\boldsymbol{r}_j|} + \sum_{i=1}^{N}V_{ext}(\boldsymbol{r}_i),\end{aligned} \tag{2.4}$$

where the nuclear part of the Hamiltonian is represented by a fixed external potential $V_{ext}(\boldsymbol{r})$

$$V_{ext}(\boldsymbol{r}) = \frac{1}{N} V_{nn}(\boldsymbol{R}) + V_{en}(\boldsymbol{r}, \boldsymbol{R}).$$

Although the Born-Oppenheimer approximation allows us to separate the degrees of freedom between electron and nucleus and to solve the nuclear part classically, the solution of the Schrodinger equation for N interacting electrons system is a formidable task since there are still the two-body mutual Coulomb interaction between these electrons. Hence, a variety of approaches have been developed to overcome this difficulty.

2.1.2 The Hartree-Fock approximation

The independent-particle approaches assume the electrons are uncorrelated except that they must obey the exclusion principle. Accordingly, the Hamiltonian of N interacting electrons (2.4) can be decoupled into N effective single-electron Hamiltonian where there is no explicit two-body term included, but we incorporated into effective potentials certain amount of the Coulomb repulsion.

Hartree in the first place proposed that the total wavefunction of N interacting electrons can be expressed as a product of N single-electron wavefunction known as the Hartree product [28-30]

$$\Psi(\boldsymbol{r_1} s_1, \boldsymbol{r_2} s_2, \dots, \boldsymbol{r_N} s_N) = \psi_1(\boldsymbol{r_1} s_1) \cdot \psi_2(\boldsymbol{r_2} s_2) \cdot \cdots \cdot \psi_N(\boldsymbol{r_N} s_N), \qquad (2.5)$$

where ψ_i denotes the spin-orbital state of one electron,

$$\psi(\mathbf{r}\mathrm{s}) = \begin{bmatrix} \psi_+(\boldsymbol{r}) \\ \psi_-(\boldsymbol{r}) \end{bmatrix}.$$

Nevertheless, this simple approximation does not handle the nature of identical particles among electrons since the Hartree product fails to satisfy the Pauli principle, which demands that the N-fermions wavefunction is antisymmetric; that is, the sign of the wavefunction changes when two of its arguments are exchanged

$$\Psi(\boldsymbol{r_1}s_1, \boldsymbol{r_2}s_2, \dots, \boldsymbol{r_i}s_i, \cdots, \boldsymbol{r_j}s_j, \cdots, \boldsymbol{r_N}s_N) = -\Psi(\boldsymbol{r_1}s_1, \boldsymbol{r_2}s_2, \dots, \boldsymbol{r_j}s_j, \cdots, \boldsymbol{r_i}s_i, \cdots, \boldsymbol{r_N}s_N). \quad (2.6)$$

To overcome this major shortcoming of the Hartree product, his students Fock and Slater, introduced the approach to ensure that the N-electron wavefunction obeys the Pauli principle is to construct a Slater determinant of orthonormal single-electron wavefunction [27]

$$\Psi(\boldsymbol{r_1}s_1, \boldsymbol{r_2}s_2, \dots, \boldsymbol{r_N}s_N) = \frac{1}{\sqrt{N!}} \begin{vmatrix} \psi_1(\boldsymbol{r_1}s_1) & \psi_1(\boldsymbol{r_2}s_2) & \cdots & \psi_1(\boldsymbol{r_N}s_N) \\ \psi_2(\boldsymbol{r_1}s_1) & \psi_2(\boldsymbol{r_2}s_2) & \cdots & \psi_2(\boldsymbol{r_N}s_N) \\ \vdots & \vdots & \ddots & \vdots \\ \psi_N(\boldsymbol{r_1}s_1) & \psi_N(\boldsymbol{r_2}s_2) & \cdots & \psi_N(\boldsymbol{r_N}s_N) \end{vmatrix}. \quad (2.7)$$

It obviously satisfies the Pauli principle of fermions because we exchange the coordinates of the space $\boldsymbol{r}$ and spin s with any two electrons, we will get a minus sign.

In order to obtain approximate solutions of the many-body stationary Schrödinger equation (2.2), the expectation value of the Hamiltonian for the N interacting electrons system (2.4) is calculated with respect to the Slater determinant wavefunction (2.7)

$$\begin{aligned} \langle \Psi | \hat{H}_e | \Psi \rangle = & \sum_{s=\uparrow,\downarrow} \sum_{i=1}^{N} \int d\boldsymbol{r} \psi_i^*(\boldsymbol{r}s) \left[-\frac{\hbar^2}{2m} \nabla^2 + V_{ext}(\boldsymbol{r}) \right] \psi_i(\boldsymbol{r}s) \\ & + \frac{1}{2} \sum_{s,s'=\uparrow,\downarrow} \sum_{i,j=1}^{N} \iint d\boldsymbol{r} d\boldsymbol{r}' \psi_i^*(\boldsymbol{r}s) \psi_j^*(\boldsymbol{r}'s') \frac{e^2}{|\boldsymbol{r}-\boldsymbol{r}'|} \psi_i(\boldsymbol{r}s) \psi_j(\boldsymbol{r}'s') \\ & - \frac{1}{2} \sum_{s,s'=\uparrow,\downarrow} \sum_{i,j=1}^{N} \iint d\boldsymbol{r} d\boldsymbol{r}' \psi_i^*(\boldsymbol{r}s) \psi_j^*(\boldsymbol{r}'s') \frac{e^2}{|\boldsymbol{r}-\boldsymbol{r}'|} \psi_j(\boldsymbol{r}s) \psi_i(\boldsymbol{r}'s'). \end{aligned} \quad (2.8)$$

The first term groups together all the one-electron terms, while the second and third terms refer to the direct and exchange interactions among electrons, respectively. We have followed

the usual practice of including the $i = j$ self-interaction, which is spurious but such terms cancel each other in the sum of direct and exchange terms.

Equation (2.8) allows us to use the variational principle to obtain better approximate wavefunction Ψ by varying orthonormal single-electron wavefunctions $\psi_i^*(\boldsymbol{r}s)$ until we minimize the ground state energy (2.8) within the given form (2.7), we can get the Hartree-Fock equation

$$\left[-\frac{\hbar^2}{2m}\nabla^2 + V_{ext}(\boldsymbol{r}) + \sum_{s'=\uparrow,\downarrow}\sum_{j=1}^{N}\int d\boldsymbol{r}'\psi_j^*(\boldsymbol{r}'s')\psi_j(\boldsymbol{r}'s')\frac{e^2}{|\boldsymbol{r}-\boldsymbol{r}'|}\right]\psi_i(\boldsymbol{r}s)$$

$$-\sum_{j=1}^{N}\int d\boldsymbol{r}'\psi_j^*(\boldsymbol{r}'s)\psi_i(\boldsymbol{r}'s)\frac{e^2}{|\boldsymbol{r}-\boldsymbol{r}'|}\psi_j(\boldsymbol{r}s) = \varepsilon_i(s)\psi_i(\boldsymbol{r}s). \qquad (2.9)$$

Equation (2.9) can be rewritten in a form analogous to many-body stationary Schrödinger equation (2.2) except that the effective one-electron Hamiltonian is an operator that depends upon the states

$$\hat{H}_i^{eff}\psi_i(\boldsymbol{r}s) = \left[-\frac{\hbar^2}{2m}\nabla^2 + \hat{V}_i^{eff}(\boldsymbol{r}s)\right]\psi_i(\boldsymbol{r}s) = \varepsilon_i(s)\psi_i(\boldsymbol{r}s) \qquad (2.10)$$

with $$\hat{V}_i^{eff}(\boldsymbol{r}s) = V_{ext}(\boldsymbol{r}) + V_H(\boldsymbol{r}) + \hat{V}_X(\boldsymbol{r}),$$

$$V_H(\boldsymbol{r}) = \sum_{s'=\uparrow,\downarrow}\sum_{j=1}^{N}\int d\boldsymbol{r}'\psi_j^*(\boldsymbol{r}'s')\psi_j(\boldsymbol{r}'s')\frac{e^2}{|\boldsymbol{r}-\boldsymbol{r}'|}, \text{ and}$$

$$\hat{V}_X(\boldsymbol{r}) = -\sum_{j=1}^{N}\int d\boldsymbol{r}'\psi_j^*(\boldsymbol{r}'s)\psi_i(\boldsymbol{r}'s)\frac{e^2}{|\boldsymbol{r}-\boldsymbol{r}'|}\cdot\frac{\psi_j(\boldsymbol{r}s)}{\psi_i(\boldsymbol{r}s)},$$

where V_H is the Hartree Coulomb potential and $\hat{V}_X$ is known as the exchange potential, so the electron-electron interaction can be reduced into effective potentials that can best mimic the real interaction. Therefore, the total energy in Hartree-Fock approximation is given by

$$E_{HF}^0 = \sum_{i=1}^{N}\varepsilon_i,$$

where ε_i is the eigenvalue of equation (2.10).

However, the electrons get often too close to each other in the Hartree-Fock scheme since the electrostatic interaction is treated through a mean-field manner. The effective Hartree-Fock potential includes the exchange effect, but does not incorporate the instantaneous repulsion between two electrons, called correlation energy. As a consequence, the long range of the Hartree-Fock exchange interaction is overestimated and much less tractable in a large system because it neglects the collective electron correlation to screen this term and to reduce the net interaction among any two electrons. This approximation therefore would yield the wrong sign and values for the work functions of simple metals. However, the DFT calculations considering the correlation energy not only show metals to be stable, but give very good quantitative agreement with experiments.

On the other hand, considering the system including N interacting electrons in some external potential and the Slater determinant wavefunction expanded with a total of N_k basis sets, the size of the Hamiltonian matrix to be diagonalized is given by

$$\frac{N_k!}{N!(N_k-N)!}. \tag{2.11}$$

This large number makes it difficultly to solve in big system size.

2.2 Density Functional Theory (DFT)

Although we can solve the stationary Schrödinger equation for N interacting electrons in an external potential approximately, it is still a difficult problem to include electron-electron interactions in the large system size.

Density functional theory (DFT), which was conceived by Walter Kohn, et al. in the

mid-1960s [31, 32], has provided the alternative independent-particle approach that incorporate effects of interaction and correlation among particles in realistic calculations. The main spirit of density functional theory is to allow for the systematic formulation of many-body problem in terms of its electron density instead of the many-body wavefunction as the basic variable. It will lead to enormous simplification since the basic variable of the system depends on only three rather than 3N degrees of freedom, no matter how large system is in three dimensions.

Accordingly, density functional theory is presently the most successful approach to calculate the electronic structure of many-body system, and it is increasingly important in the quantum chemistry, condensed matter physics, and even nanoscale device physics.

2.2.1 The Hohenberg-Kohn Theorem

What is truly remarkable is that all physical properties of the system can in principle be determined with the knowledge only of the ground-state density. This is precisely the statement of the Hohenberg-Kohn theorem[31]. The intuitive version of Hohenberg-Kohn theorem states that given any density $n(\mathbf{r})$ as the ground-state density for some N-electron system, the Hamiltonian of that system is then uniquely determined, and so then are all the eigenstates and the expectation value of any operator.

The proof of this theorem can be accomplished of the system with non-degenerate ground states, and the Hamiltonian for the N interacting electrons in an external potential is described by (2.4). Let us assume that two external potentials V_{ext} and V'_{ext} differing by more than a trivial constant can give rise to the same ground-state density $n(\mathbf{r})$. Obviously, distinct Hamiltonian $\hat{H}$ and $\hat{H}'$ due to different V_{ext} and V'_{ext} will lead to distinct ground-state wavefunction Ψ_0 and Ψ'_0, respectively.

According to the variational principle, we have

$$\varepsilon_0 = \langle \Psi_0 | \hat{H} | \Psi_0 \rangle < \langle \Psi_0' | \hat{H} | \Psi_0' \rangle, \tag{2.12}$$

where ε_0 is the ground-state energy of $\hat{H}$. Then we can rewrite (2.12) by the relation between $n_o(\boldsymbol{r})$, $V_{ext}(\boldsymbol{r})$, and $\langle \Psi_0 | V_{ext} | \Psi_0 \rangle$

$$\langle \Psi_0 | V_{ext} | \Psi_0 \rangle = \int n_o(\boldsymbol{r}) V_{ext}(\boldsymbol{r}) d\boldsymbol{r}, \tag{2.13}$$

so that

$$\begin{aligned} \varepsilon_0 < \langle \Psi_0' | \hat{H} | \Psi_0' \rangle &= \langle \Psi_0' | \widehat{H'} + V_{ext} - V_{ext}' | \Psi_0' \rangle \\ &= \varepsilon_0' + \int n_0'(\boldsymbol{r}) [V_{ext}(\boldsymbol{r}) - V_{ext}'(\boldsymbol{r})] d\boldsymbol{r}. \end{aligned} \tag{2.14}$$

An analogous argument, obtained by interchanging primed and unprimed quantities yields

$$\begin{aligned} \varepsilon_0' < \langle \Psi_0 | \widehat{H'} | \Psi_0 \rangle &= \langle \Psi_0 | \hat{H} + V_{ext}' - V_{ext} | \Psi_0 \rangle \\ &= \varepsilon_0 + \int n_o(\boldsymbol{r}) [V_{ext}'(\boldsymbol{r}) - V_{ext}(\boldsymbol{r})] d\boldsymbol{r}. \end{aligned} \tag{2.15}$$

Add the above two equations, and using our assumption that $n_0'(\boldsymbol{r}) = n_o(\boldsymbol{r})$ then leads to the following contradiction

$$\varepsilon_0 + \varepsilon_0' < \varepsilon_0 + \varepsilon_0',$$

As a result, there cannot be two different external potentials that come with the same ground-state density. In other words, it follows that two identical ground-state densities must stem from identical external potentials, and with that our proof of the Hohenberg-Kohn theorem is complete.

There is also an important variational principle associated with the Hohenberg-Kohn theorem. Since the ground-state energy ε_0 is uniquely determined by ground-state density

n_o, the variational principle establish that

$$\varepsilon_0 < \varepsilon[n'] \equiv \langle \Psi_0[n'] | \hat{H} | \Psi_0[n'] \rangle \quad for\; n' \neq n_o. \tag{2.16}$$

Therefore, the ground-state density n_o can be determined by varying the density n' to minimize the energy $\varepsilon[n']$.

2.2.2 The Kohn-Sham Formulation

While Hohenberg-Kohn theorem rigorously establishes that we may only use the electron density as a variable to find the ground-state energy of an interacting N-electron problem, it does not provide us with any useful computational scheme. This is provided by the Kohn-Sham formalism [32]. The idea here is to use a non-interacting auxiliary system and to look for an external potential V_s such that the non-interacting system has the same ground-state density as the real interacting system.

Let us start by considering a non-interacting N-electron system in an external potential V_s. The Hamiltonian $\hat{H}_S$ of this system is given by

$$\hat{H}_S = \hat{T} + \mathrm{V_s}. \tag{2.17}$$

Then we apply the Hohenberg-Kohn theorem to this system. Accordingly, there exists a unique energy functional

$$\begin{aligned} \varepsilon_s[n] &= \langle \Psi_0^s[n] | \hat{H}_S | \Psi_0^s[n] \rangle = \langle \Psi_0^s[n] | \hat{T} + V_s | \Psi_0^s[n] \rangle \\ &= T_s[n] + \int V_s(\boldsymbol{r}) n(\boldsymbol{r}) d\boldsymbol{r}, \end{aligned} \tag{2.18}$$

where $T_s[n]$ is the kinetic energy functional of a system of N non-interacting electrons.

The ground-state density of this system is easily obtained. It is simply

$$n_s(\boldsymbol{r}) = \sum_{i=1}^{N} |\phi_i(\boldsymbol{r})|^2, \tag{2.19}$$

where we have occupied the N single-particle states $\phi_i(\boldsymbol{r})$, which satisfy the single-electron Schrödinger equation

$$\left[-\frac{\hbar^2}{2m}\nabla^2 + V_s(\boldsymbol{r})\right]\phi_i(\boldsymbol{r}) = \varepsilon_i\phi_i(\boldsymbol{r}), \quad \varepsilon_1 \le \varepsilon_2 \le \cdots, \tag{2.20}$$

and have the N lowest eigenvalue ε_i.

But we are really interested in a system of N interacting electrons in an external potential V_{ext}, we would determine the form that V_s must take in order for the non-interacting system to have the same ground-state density as the interacting system in the external potential V_{ext}. The strategy we use is to solve for the density using the auxiliary non-interacting system, and then insert this density into an approximate expression for the total energy of the interacting system.

The first step in this process is to rewrite the energy functional of the interacting system, which was given in (2.18), as

$$\begin{aligned}
\varepsilon[n] &= \langle \Psi_0[n]|\hat{H}|\Psi_0[n]\rangle = \langle \Psi_0[n]|\hat{T} + \hat{V} + V_{ext}|\Psi_0[n]\rangle \\
&= T[n] + V[n] + \int n(\boldsymbol{r})V_{ext}(\boldsymbol{r})\,d\boldsymbol{r} \\
&= T_s[n] + \left\{T[n] - T_s[n] + V[n] - \frac{e^2}{2}\iint \frac{n(r)n(r')}{|r-r'|}\,d\boldsymbol{r}d\boldsymbol{r}'\right\} \\
&\quad + \frac{e^2}{2}\iint \frac{n(r)n(r')}{|r-r'|}\,d\boldsymbol{r}d\boldsymbol{r}' + \int n(\boldsymbol{r})V_{ext}(\boldsymbol{r})\,d\boldsymbol{r} \\
&= T_s[n] + \frac{e^2}{2}\iint \frac{n(r)n(r')}{|r-r'|}\,d\boldsymbol{r}d\boldsymbol{r}' + \int n(\boldsymbol{r})V_{ext}(\boldsymbol{r})\,d\boldsymbol{r} + \varepsilon_{XC}[n].
\end{aligned} \tag{2.21}$$

We have then defined the sum of the terms in braces to be the exchange-correlation

energy functional $\varepsilon_{XC}[n]$

$$\varepsilon_{XC}[n] \equiv T[n] - T_s[n] + V[n] - \frac{e^2}{2} \iint \frac{n(\boldsymbol{r})n(\boldsymbol{r}')}{|\boldsymbol{r}-\boldsymbol{r}'|} d\boldsymbol{r} d\boldsymbol{r}'. \tag{2.22}$$

We have thus swept all our ignorance about electron interactions beyond the Hartree term under the rug that we call $\varepsilon_{XC}[n]$. What we gain in writing $\varepsilon_{XC}[n]$ in this way is that we can eventually focus on developing reasonable approximations for $\varepsilon_{XC}[n]$.

According to the Hohenberg-Kohn theorem, the density n that minimizes the functional $\varepsilon[n]$ is the ground-state density. Thus by taking the variation of (2.21) with respect to the density we obtain

$$\frac{\delta\varepsilon[n]}{\delta n(\boldsymbol{r})} = \frac{\delta T_s[n]}{\delta n(\boldsymbol{r})} + e^2 \int \frac{n(\boldsymbol{r}')}{|\boldsymbol{r}-\boldsymbol{r}'|} d\boldsymbol{r}' + V_{ext}(\boldsymbol{r}) + v_{XC}[n(\boldsymbol{r})] = 0, \tag{2.23}$$

where we have formally defined the exchange-correlation potential as

$$v_{XC}[n(\boldsymbol{r})] \equiv \frac{\delta\varepsilon_{XC}[n(\boldsymbol{r})]}{\delta n(\boldsymbol{r})}.$$

We now use the auxiliary non-interacting system and its Schrödinger equation, from which we can similarly show that

$$\frac{\delta T_s[n]}{\delta n(\boldsymbol{r})} + V_s(\boldsymbol{r}) = 0. \tag{2.24}$$

By comparing this result with (2.23) we see that this effective potential $V_s(\boldsymbol{r})$ must satisfy

$$V_s(\boldsymbol{r}) = V_{ext}(\boldsymbol{r}) + e^2 \int \frac{n(\boldsymbol{r}')}{|\boldsymbol{r}-\boldsymbol{r}'|} d\boldsymbol{r}' + v_{XC}[n(\boldsymbol{r})]. \tag{2.25}$$

We are now in a position to implement the self-consistent Kohn-Sham scheme. We first choose an initial trial form of the function $n(\boldsymbol{r})$ and substitute into (2.15) to find a trial form of V_s. We then solve (2.20) for the single-particle wavefunction $\phi_i(\boldsymbol{r})$, and use (2.19) to find

$n(\boldsymbol{r})$ out of the next iteration. The equations are then solved again, and this process is repeated until self-consistency is obtained, i.e., until the input and output density in one iteration are sufficiently close to one another.

2.3The Exchange-correlation functional

In the Kohn-Sham formulism for DFT, the total energy written as (2.21) may be found that the exchange-correlation energy functional plays the important role of the self-consistent calculation since all components of (2.21) are known exactly with the notable exception of this term. Before we can actually implement the Kohn-Sham formalism, we have to introduce some workable approximation for the exchange-correlation energy ε_{XC}.

Conventionally, the exchange-correlation energy is separated into exchange and correlation parts

$$\varepsilon_{XC}[n] = \varepsilon_X[n] + \varepsilon_C[n]. \quad (2.26)$$

Next, we are going to introduce some approximations for the exchange-correlation energy using in our calculations.

2.3.1 The local density approximation (LDA)

The first such approximation to be suggested was the Local Density Approximation (LDA) [32]. The idea behind the LDA is a uniform electron gas. In the LDA, we assume that the density of inhomogeneous system varies very slowly, so that the exchange-correlation energy is locally that of a homogeneous system at the local density. Therefore, the difficulty is avoided with the assumption that v_{XC} depends only on the local density $n(\boldsymbol{r})$, and that $\varepsilon_{XC}[n]$ can thus be written as

$$\varepsilon_{XC}^{LDA}[n] = \int \epsilon_{XC}[n]n(\boldsymbol{r})d\boldsymbol{r}, \tag{2.27}$$

where $\epsilon_{XC}[n]$ is the exchange-correlation energy per particle of a homogeneous system of density n.

Although no general form is known to exactly determine $\epsilon_{XC}[n]$, the low-density and high-density limits can be calculated analytically. Usually, the density is expressed in terms of the dimensionless parameter r_s, which is the radius of the sphere that can be assigned to each electron in average, measured in units of the Bohr radius a_0. This is

$$r_s = \left(\frac{4\pi {a_0}^3}{3}n\right)^{-1/3}. \tag{2.28}$$

The exchange energy per particle is straightforward to calculate by Bloch and Dirac in the late 1920's [33], and the result is

$$\epsilon_X(n) = -\frac{3}{4\pi}\left(\frac{9\pi}{4}\right)^{1/3}\frac{e^2}{r_s a_0}. \tag{2.29}$$

No such explicit expression is known for the correlation energy per particle ϵ_C. However, a popular approximation for the correlation energy is based on highly accurate numerical quantum Monte-Carlo simulations of the homogeneous electron gas for certain values of r_s by Ceperley and Alder [34]. These are then parameterized. Perdew and Zunger use a Pade approximation in ${r_s}^{1/2}$ for low-density case $r_s \geq 1$ [35]:

$$\epsilon_C = \frac{\gamma}{1+\beta_1\sqrt{r_s}+\beta_2 r_s} \tag{2.30}$$

with $$\gamma = -0.1423\frac{e^2}{a_0}, \quad \beta_1 = 1.0529, \quad \beta_2 = 0.3334.$$

This form is then joined smoothly to the high-density form of ϵ_C for $r_s \leq 1$, which is

$$\epsilon_C = A \ln r_s + B + C r_s \ln r_s + D r_s \qquad (2.31)$$

with (all parameters given in units of $\frac{e^2}{a_0}$)

$$A = 0.0311, \quad B = -0.048, \quad C = 0.0020, \quad D = -0.0166.$$

Practice shows that LDA yields adequate ground-state properties even for strongly inhomogeneous systems since the errors from exchange and correlation parts cancel partially. The LDA not only yield the accurate work functions of the simple metals, but also gives bond lengths of molecules and solids typically with an astonishing accuracy of ~2%. However, the moderate accuracy that LDA delivers is certainly insufficient for most applications in chemistry.

2.3.2 The generalized gradient approximation (GGA)

An obvious way to go beyond the LDA is the gradient expansion approximation (GEA) which extends the exchange-correlation functional with terms containing gradients of the electron density.

However, it does not lead to consistent improvement over the LDA since the second-order GEA is found to violate the sum rule and the non-positivity constraint on the exchange hole, both of which are important physical conditions [36]. The question then arises of whether one can construct a gradient expansion that avoids these shortcomings, so that the resulting exchange-correlation hole satisfies the most important sum rules.

The resulting gradient corrections with exchange-correlation hole constraints restored are referred to as Generalized Gradient Approximations (GGAs). The exchange-correlation energy in the GGA is written as

$$\varepsilon_{XC}^{GGA}[n^{\uparrow},n^{\downarrow}] = \int f(n^{\uparrow},n^{\downarrow},\nabla n^{\uparrow},\nabla n^{\downarrow})d\boldsymbol{r}. \tag{2.32}$$

Perdew and Wang have developed a GGA functional based on real-space cutoff of the spurious long-range components of the second-order gradient expansion for the exchange-correlation hole [37], and then improved by the PBE (Perdew-Burke-Enzerhof) form including an accurate description of the linear response of the uniform electron gas, correct behavior under uniform scaling, and a smoother potential [38].

The PBE functional for exchange energy is given by

$$\varepsilon_{X}^{GGA}[n^{\uparrow},n^{\downarrow}] = \int n(\boldsymbol{r})\epsilon_{X}^{unif}(n)F_X(s)d\boldsymbol{r}, \tag{2.33}$$

where $\epsilon_X^{unif}(n) = -\frac{3e^2k_F}{4\pi}$ is the Slater exchange energy density in the uniform electron gas approximation, $k_F = [3\pi^2 n]^{1/3}$ is the local Fermi wave vector, and $F_X(s)$ is the enhancement factor depending on a dimensionless density gradient s defined as $s = \frac{|\nabla n|}{2k_F n}$.

For the linear response of uniform electron gas, LDA is an excellent approximation while GEA is not. In order to recover the LDA linear response, the enhancement factor of the exchange functional takes the form

$$F_X^{PBE}(s) = 1 + \kappa - \frac{\kappa}{1+\frac{\mu}{\kappa}s^2}, \tag{2.34}$$

where $\kappa = 0.804$ is set to the maximum value allowed by the local Lieb-Oxford bound on the exchange-correlation energy and $\mu = 0.21951$ is chosen to recover the linear response of the uniform gas such that the effective gradient coefficient for exchange cancels that for correlation.

The form of the PBE functional for correlation energy is expressed as the local

correlation plus an additive term both of which depend upon the gradients and the spin polarization.

$$\varepsilon_C^{GGA}[n^\uparrow, n^\downarrow] = \int n(\boldsymbol{r})\left[\epsilon_C^{unif}(r_s, \xi) + H(r_s, \xi, t)\right] d\boldsymbol{r}, \tag{2.35}$$

where r_s is the local Seitz radius as shown by (2.28), $\xi = \frac{n^\uparrow - n^\downarrow}{n}$ is the relative spin polarization, and $t = \frac{|\nabla n|}{2\phi k_s n}$ is a dimensionless density gradient. Here $\phi(\xi) = \left[(1+\xi)^{2/3} + (1-\xi)^{2/3}\right]/2$ is a spin-scaling factor, and k_s is the Thomas-Fermi wave vector.

Then, the gradient contribution H is constructed from the slowly varying limit, the rapidly varying, and uniform density scaling condition.

$$H(r_s, \xi, t) = \frac{e^2}{a_0}\gamma\phi^3 \, ln\left(1 + \frac{\beta}{\gamma} t^2 \cdot \frac{1 + At^2}{1 + At^2 + A^2 t^4}\right), \tag{2.36}$$

where

$$A = \frac{\beta}{\gamma}\left[exp\left(\frac{-\epsilon_C^{unif}}{\gamma\phi^3 \frac{e^2}{a_0}}\right) - 1\right]^{-1}.$$

The great strength of the GGA lies in the dramatic improvement it gives over the LDA in calculating such properties as bond dissociation energies, which the LDA may overestimate by as much as 100%, while the GGA gives errors typically of the order of ten percent or less. With modern GGA exchange-correlation potentials, atomic and molecular quantities can now be calculated with chemical accuracy.

2.3.3 Hybrid functionals

Unfortunately, the DFT calculations cannot correctly predict the electronic structure of

semiconductor materials since the bandgap is considerably underestimated with the aforementioned exchange-correlation energy functional such as LDA and GGA. Recently, this problem can be solved by a new class of DFT exchange-correlation functional which is named hybrid functional.

Hybrid functionals are a class of approximations to the exchange-correlation energy functional in DFT that incorporate a portion of exact exchange from Hartree-Fock approximation. However, the Hartree-Fock exchange in hybrid DFT calculations is much less tractable in large systems arising from the slow decay of the exchange interaction with distance.

Screened Coulomb hybrid functional proposed by Heyd et al. can accelerate the decay of the Hartree-Fock exchange interaction by substituting the full *1/r* Coulomb potential with a screened potential which decomposes of the exchange interaction into the short range (SR) and long range (LR) components [39].

$$\varepsilon_X^{HSE} = \mathrm{a}\left[\varepsilon_X^{HF,SR}(\omega) + \varepsilon_X^{HF,LR}(\omega)\right] + (1-a)\left[\varepsilon_X^{PBE,SR}(\omega) + \varepsilon_X^{PBE,LR}(\omega)\right], \quad (2.37)$$

where the mixing coefficient a = 1/4 is determined by perturbation theory [40] and ω is the screening parameter governing the extent of short range interactions.

Numerical tests based on the particular value of screening parameter indicate that the Hartree-Fock and PBE long range exchange contributions to this functional are rather small, and that these terms tend to cancel each other. As a result, we obtain the HSE screened Coulomb potential hybrid density functional of the form

$$\varepsilon_{XC}^{HSE} = \left[\frac{1}{4}\varepsilon_X^{HF,SR}(\omega) + \frac{3}{4}\varepsilon_X^{PBE,SR}(\omega)\right] + \varepsilon_X^{PBE,LR}(\omega) + \varepsilon_C^{PBE}(\omega). \quad (2.38)$$

The optimal value of the above screening parameter ω in the recent implementation is $\omega = 0.207\ \text{Å}^{-1}$, designated as HSE06, instead of the earlier suggested value $\omega = 0.3\text{Å}^{-1}$ since HSE06 functional yields better thermochemical results than the original implementation and preserves the good accuracy for bandgaps and lattice constants in solids. Due to the inclusion of the screened Coulomb interaction, the computational time needed for HSE is within a factor of two to four of LDA or GGA calculations.

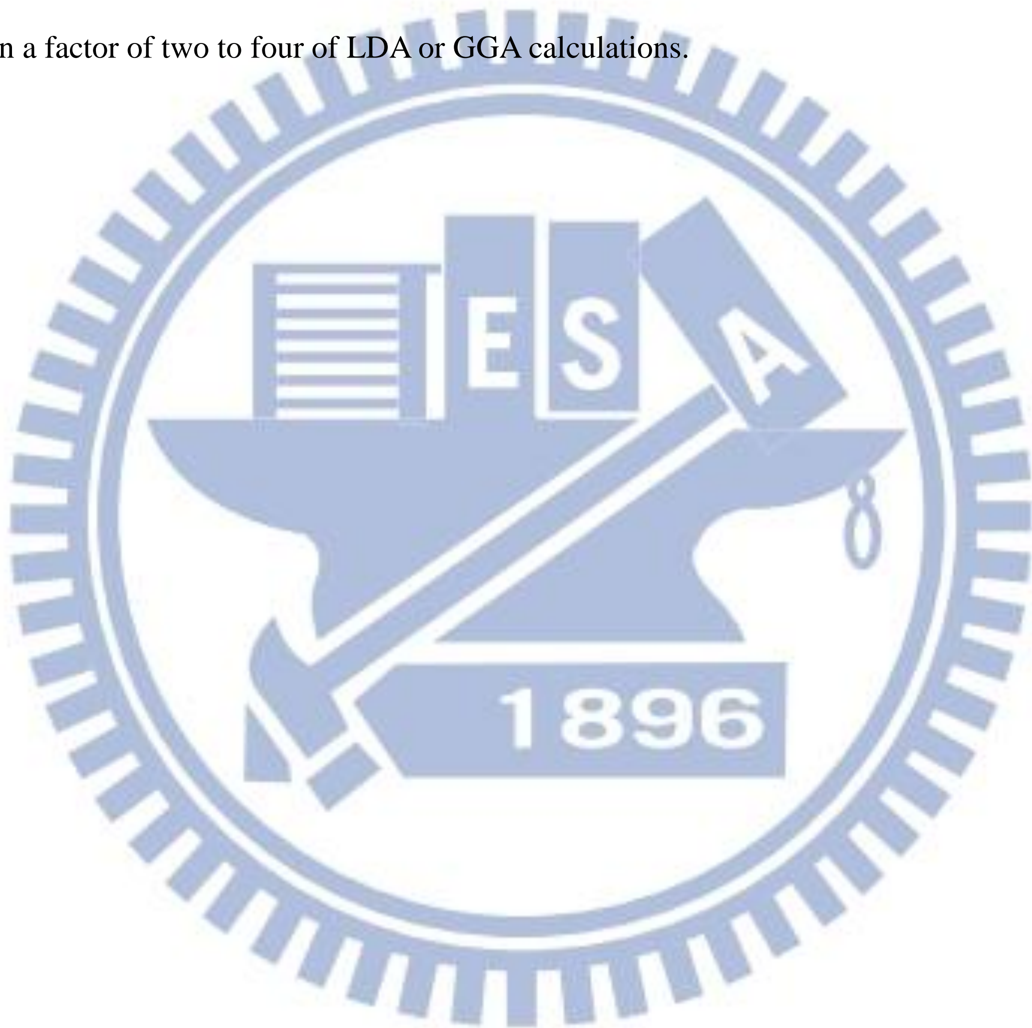

Chapter 3 Results and Discussion

The experimental lattice constant of the Ge bulk is a=5.658 Å in a diamond type lattice as shown in Figure 3-1, which consists of two interpenetrating face-centered cubic Bravais lattices, displaced along the body diagonal of the cubic cell by one quarter the length of the diagonal.

NiGe crystallizes in a MnP type lattice with space group Pnma (#62 in the International X-Ray Table). There are four symmetry-equivalent Ni and four symmetry-equivalent Ge atoms per primitive orthorhombic cell depicted in Figure 3-2. The experimental lattice constants of the NiGe bulk are a=5.381 Å, b=3.428 Å, and c=5.811 Å in the primitive orthorhombic structure.

3.1 Choosing Exchange-correlation Functional

In order to determine the best exchange-correlation functional to be used in this work, we first obtain the Ge bulk with various exchange-correlation functionals and then examine their calculated band structures using those calculated lattice constants. We show in Table 3-1 that the LDA functional [41] yields the best lattice constant for the Ge bulk, and using this best lattice constant a=5.645 Å, we figure out that only HSE06 hybrid functional gives rise to a Ge bandgap that agrees excellently with the experimental value 0.785 eV at zero temperature [42]. The Ge band structure calculated by HSE06 hybrid functional is shown in Figure 3-3, compared with the photoemission experiments at the high-symmetry points [43]. As one expects, the HSE06 hybrid functional dispersions are very close to the experimental observations. By also using LDA, the NiGe lattice constants are calculated to be a=5.245 Å, b=3.425 Å, and c=5.715 Å, which are slightly less than the experimental values.

Based on the above bulk studies, we will use LDA to relax the atomic structures and then HSE06 to calculate the electronic structures of the NiGe/Ge interface structures.

3.2 Structural Modeling of the NiGe/Ge Contact

Before studying the effects of dopant segregation around the NiGe/Ge interface theoretically, we must construct the atomic structure consistent with our experimental sample (courtesy of Che-Ju Shih)[44]. The sample is grown by sputtering 10-nm-thick Ni on the lightly-doped n-type Ge region and annealing at 350°C for 5 minutes by a backend vacuum annealing furnace to form germanide. The detailed process flow is shown in Figure 3-4.

The XRD diffraction spectrum of the NiGe/Ge structure in Figure 3-5 shows that the NiGe film is polycrystalline and the dominating crystalline phases are (112), (210), and (111) orientations. Therefore, we consider the preferred alignment of NiGe(112), NiGe(210), and NiGe(111) lattice planes with Ge(001) plane in the substrate since the grain sizes of crystalline phases are about 10 nm [45] which is equivalent to the thickness of the NiGe film in our sample.

It is difficult to build the NiGe slab including three different phases, so we simplify the realistic NiGe film by considering NiGe(112), (210), and (111) phases separately. Then, we construct three kinds of NiGe slabs by cleaving the NiGe bulk along (112), (210), and (111) plane, respectively.

In constructing the NiGe/Ge interface structure, we must match the lattice constants of the two materials along the interface by choosing a suitable in-plane cell size that provides enough calculation accuracy by consuming a reasonable amount of computing resource. The two lateral surface vectors U and V on the above interface plane are shown in Table 3-2, 3-3,

and 3-4, for different NiGe surface orientations. The above mentioned cell shapes is mapped on the Ge(001) surface, as illustrated in Figure 3-6. Given that the Ni-Ge metallic bond is weaker than the covalent Ge-Ge, the NiGe slabs are relaxed to match the fixed lateral cell size of Ge(001) slabs. Following the above procedures and considerations, we can successfully construct the NiGe(112)/Ge(001), NiGe(210)/Ge(001), and NiGe(111)/Ge(001) interface structures.

Nevertheless, the cell size of the NiGe(210)/Ge(001) and NiGe(111)/Ge(001) interface structures are too large beyond our computability to calculate the electronic structures using HSE06 functional. Hence, the realistic polycrystalline NiGe film is represented for the subsequent calculations by merely considering NiGe(112) phase, which is the highest diffraction peak in the XRD analysis of NiGe film.

There are two different surface terminations of the NiGe(112) slab, as shown in Figure 3-7 and 3-8, respectively. One of the termination types, hereby called NiGe(112)T4 slab, contains 4 atoms (2 Ni and 2 Ge atoms) per lateral unit cell, while the other type, NiGe(112)T8, has 8 atoms (4 Ni and 4 Ge atoms).

To compare the stability of not only the two termination types but also by sliding NiGe and Ge slabs along the interface, we put the NiGe and Ge slabs together with various choices of lateral matching for both terminations, as shown in Figure 3-9. The total energies of all the configurations we tried are separately listed in Table 3-5 and Table 3-6.

The results in Table 3-5 show that the NiGe(112)/Ge(001) interface structure becomes the most stable when the NiGe slab is terminated at the above-mentioned T4 with the Ni of NiGe being matched to the Ge of Ge(001). This particular configuration of the NiGe/Ge interface structure will be used all though the rest of this thesis.

In summary, the NiGe/Ge contact is simulated by a supercell connecting 8 NiGe(112)T4 layers, 16 Ge(001) layers, and 12Å -vacuum where the dangling bonds of the Ge surface are saturated by H atoms as shown in Figure 3-10.

3.2.1 Behaviors of Segregated Dopant around the Interface

Before exploring whether the n-type dopant such as phosphorous and arsenic can be segregated and pile-up at the NiGe/Ge interface or not, we first assume that the implanted dopant is activated and migrates into the substitutional sites. Therefore, we replace one at a time of the Ge atoms around the interface by a doping atom in the NiGe/Ge interfacial structure as shown in Figure 3-10 and then relax the doped interfacial structure by the DFT-LDA calculations until the forces are less than 0.01eV/Å for atoms within 9 Å from the interface, where the atoms beyond this region approach their corresponding bulk positions. The total energy of the system with one Ge atom being substituted for a phosphorous and arsenic is shown in Figure 3-11 and Figure 3-12, respectively.

The result in Figure 3-11 shows that the phosphorous doping occurs most stably at the positions labeled as MG3 and SG1a in Figure 3-10. It implies that the phosphorous dopant can be segregated around the NiGe/Ge interface and piled up on the NiGe side. Nevertheless, the arsenic atom prefers to stay on the Ge side near the interface as shown in Figure 3-12 since the Ge-side doping of arsenic is more stable than the NiGe-side. The most stable substitutional site for the arsenic dopant is labeled as SG1c in Figure 3-10. To sum up, although both phosphorous and arsenic dopants can be segregated around the NiGe/Ge interface in our calculations, the former prefer to pile up on the NiGe side but the latter like to stay on the Ge side around the interface. The above results are consistent with the SIMS analysis of the experiment as shown in Figure 3-13 and Figure 3-14 [23].

After understanding the behaviors of segregated dopant around the interface, we propose that phosphorous would be a better choice for the implantation before NiGe (IBG) process since phosphorous atoms are difficult to diffusion from the NiGe side to the Ge due to the high barrier. Nevertheless, arsenic atoms can migrate into the Ge side either IBG or implantation after NiGe (IAG) process.

3.2.2 Barrier Height Modified by Dopant Segregation

To find out how thick the Ge slab we need to approach the bulk limit. We separately calculate the 12-layers, 16-layers, and 20-layers Ge(001) slab with 12-Å vacuum where the surface dangling bonds are saturated by H atoms.

One can see that the bandgap of the pure Ge(001) slab is a function of the number of atomic layers, as shown in Figure 3-15. As the number of the Ge(001) layers keeps increasing, We expect the calculated bandgap of the Ge slab would converge to the bulk limit. Since the NiGe/Ge contact is simulated by a supercell including 16 Ge(001) layers, we must calibrate this size-effect of the gap, and consequently we scale the gap by a factor of 0.781/1.292 (Ge-bulk bandgap divided by the 16 Ge(001) layers) to compare with the experimental Schottky barrier height of the NiGe/Ge contact.

On the other hand, we can easily obtain the orbital component of the Ge conduction band by the partial density of states (PDOS) of the Ge atom in the pure 16-layers Ge(001) slab which does not have any interface state. The result shows that the conduction band of the Ge atoms carries 3d components as shown in Figure 3-16. Based on the above, we can accurately determine the position of the physical conduction band edge (CBE).

At first, we calculate the undoped NiGe/Ge interfacial structure by the DFT calculations

using the HSE06 functional. Since the a significant number of interface states spread across the Ge bandgap when looking close to the interface, and this bothers us in determining the Schottky barrier height, we have to choose the PDOS of the Ge atom in a layer sufficiently far away such that the interface states become negligible. The calculated PDOS of the Ge atom labeled as SG9b in Figure 3-10 is shown in Figure 3-17. The result shows that the energy difference between the Fermi level and the physical conduction band edge is 1.041 eV and the value calibrated by a scaling factor is 0.629 eV, which is comparable with the experimental result.

Subsequently, we investigate three different doping cases: the phosphorous at the most stable position, phosphorous at the metastable, and the arsenic doped at the most stable site, respectively. For all those cases, we plot the Ge-side PDOS shown in Figure 3-18, 3-19, and 3-20, where we specifically pick the Ge atom labeled as SG9b (see Figure 3-10) for PDOS.

The result in Figure 3-18 shows that doping phosphorous on the NiGe side does not modify Schottky barrier height since the energy difference between the Fermi level and the physical conduction band edge is 1.069 eV, very close to the undoped case. The above result can be understood in the way that doping phosphorous does not yield more valence electrons to occupy higher states since it replaces the Ge atom of the metallic Ni-Ge bond instead of the covalent Ge-Ge bond. Therefore, the position of the Fermi level in this case is not change.

Subsequently, we explore the case of doping phosphorous on the Ge side, which is the metastable segregated site in the NiGe/Ge interfacial structure. The result in Figure 3-19 shows that the energy difference between the Fermi level and the physical conduction band edge decreases to 0.933 eV. It implies that the Schottky barrier height of the NiGe/Ge contact can be modified from the undoped 0.629 eV to the doped 0.563 eV by Ge-side doping of

Phosphorous.

Finally, the result of the arsenic doped at the most stable segregated position (on the Ge side) is similar to the case of doping phosphorous on the Ge side as shown in Figure 3-20. It shows that the energy difference between the Fermi level and the physical conduction band edge reduces to 0.906 eV. After doing the calibration, we figure out that the arsenic doping suppress the Schokkty barrier height from 0.629 eV to 0.548 eV. Therefore, the dopant segregation using conventional n-type dopant such as phosphorous and arsenic is not very effective to modify the Schottky barrier height of the NiGe/Ge contact but the arsenic on the Ge side is slightly better than using phosphorous doping. Those results imply that the improvement of the NiGe/Ge junction characteristics in Figure 3-21 and 2-22 [44] are mainly attributed to the increase of doping concentration due to dopant segregation and partially attributed to the reduction of the physical Schottky barrier height.

The above two results can be interpreted by the fact that the Fermi level is increased and pinned at another energy since the dopant by replacing one Ge atom of the covalent Ge-Ge bonding can produce more valence electrons to occupy higher states.

3.3 Effect of Nitrogen Dopant Segregated on the NiGe/Ge Contact

The insignificant reduction of the physical Schottky barrier height caused by segregation of the conventional dopants such as phosphorous and arsenic, we further using different dopants that were claimed to lower the Schottky barrier height drastically in Si-based junction. Jing Guo, et al. have calculated the nitrogen dopant segregation in the CoSi2/Si(100) structure. They assert it will reduce the Schottky barrier height from 0.66 eV to 0.14 eV, but so far there has not been any experiments published to justify their results [46]. We will also explore the

physical mechanism of the modified electron Schottky barrier height on the Ge-based contact with dopant segregation by inspecting the different orbital contributions between the interface states and conduction band.

In view of the above mentioned analysis, we investigate the change of the Schottky barrier height on the NiGe/Ge(001) contact by dopant segregation using nitrogen atom. The nitrogen-doped interfacial structure is constructed in Figure 3-10 by replacing one Ge atom by nitrogen at the position labeled as SG9b, which turns out to be the most stable segregated position after we try out different doping positions around the interface. By also using HSE06 hybrid functional, we obtain the electronic structure of this interfacial structure.

The calculated PDOS of the Ge atom at the 9th layer away from the interface is depicted in Figure 3-23. The results show that the effective conduction band edge is closer to the Fermi level since the physical conduction band edge is extended by the interface states, which are almost no 3*d* orbital components. However, we need to study in depth whether the physical Schottky barrier height is reduced or not due to decreasing the energy difference between the Fermi level and the effective conduction band edge from 0.983 eV to 0.26 eV.

In order to see how far the interface state can survive away from the interface, we make additional plots of the calculated PDOS of the Ge atom of the 1st, 5th, and 13th layers from the interface, as shown in Figure 3-24, 3-25, and 3-26, respectively. It is obvious that the interface states disappear at the 13th Ge layer, and the effective conduction band edge is returned to the physical conduction band edge, which is 0.983 eV above the Fermi level.

According to above results, we conclude that the method of dopant segregation using nitrogen dopant is almost no effect to modify the Schottky barrier height on the NiGe/Ge contact since the energy difference between the Fermi level, and the physical conduction band

edge is nearly no change. Although the nitrogen dopant can be segregated around the interface and yield a large number of the interface states spreading the Ge bandgap, but the interface state tails can survive from only up to 17 Å . Therefore, the electron Schottky barrier height is still the energy difference between the Fermi level and the bulk conduction band edge as show in Figure 3-27.

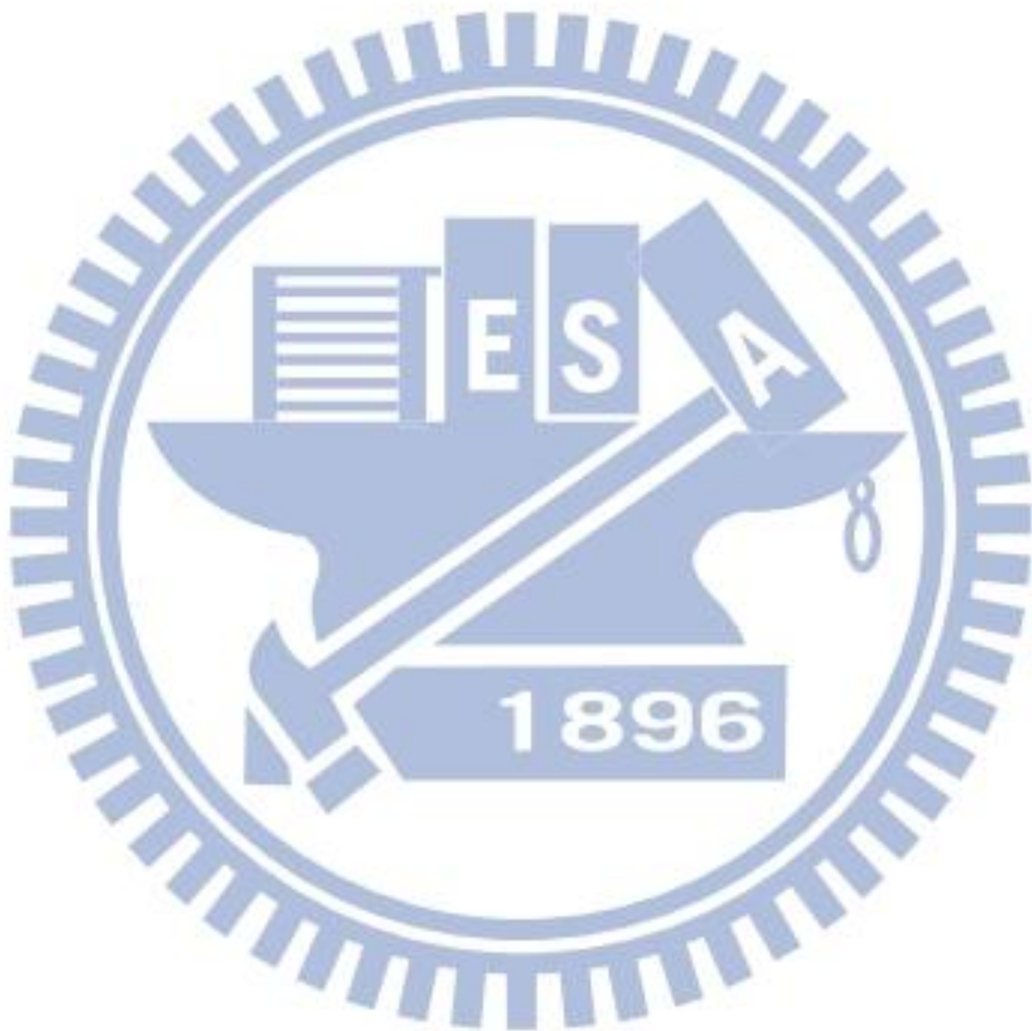

Table 3-1 Calculated lattice constant (second row) and also the Ge-bulk bandgap (fourth to eighth rows) at the various lattice constant using different exchange-correlation functionals. The experimental lattice constant and bandgap are 5.658 Å and 0.785 eV [42], respectively.

Exchange-correlation functional	LDA	GGA-PW91	GGA-PBE	HSE06
Lattice constant (Å)	5.645	5.771	5.777	5.710
	Ge bandgap (eV)			
5.645	No gap	0.107	0.124	0.781
5.771	No gap	No gap	No gap	0.193
5.777	No gap	No gap	No gap	0.157
5.710	No gap	No gap	No gap	0.522
5.658	No gap	0.042	0.058	0.755

Table 3-2 Specific lateral surface vectors chosen for the NiGe(112)/Ge(001) interface strucutre.

	U(h k l)	V(h k l)	Length U (Å)	Length V (Å)	Angle (°)	Volume (cell)
NiGe(112) slab	1 -1 0	1 1 -1	6.265	8.480	72.717	1.0
Ge(001) slab	1 0 0	0.5 1.5 0	5.645	8.925	71.565	1.5
NiGe(112)/Ge(001) mismatch			10.983%	4.986%	1.152°	

Table 3-3 Specific lateral surface vectors chosen for the NiGe(210)/Ge(001) interface strucutre.

	U(h k l)	V(h k l)	Length U (Å)	Length V (Å)	Angle (°)	Volume (cell)
NiGe(210) slab	0 0 1	2 -4 0	5.715	17.256	90	2.0
Ge(001) slab	1 0 0	0 3 0	5.645	16.934	90	3.0
NiGe(210)/Ge(001) mismatch			1.240%	1.901%	0°	

Table 3-4 Specific lateral surface vectors chosen for the NiGe(111)/Ge(001) interface strucutre.

	U(h k l)	V(h k l)	Length U (Å)	Length V (Å)	Angle (°)	Volume (cell)
NiGe(111) slab	1 -1 0	-2 4 -2	6.265	20.698	141.84	2.0
Ge(001) slab	1 0 0	-3 2 0	5.645	20.352	146.31	2.0
NiGe(111)/Ge(001) mismatch			10.983%	1.700%	4.470°	

Table 3-5 Total energy of the various choices of lateral matching with NiGe(112)T4 and Ge(001) slabs.

0.5	-260.955844	-260.923771	-261.578593	-262.260734
0.25	-260.219115	-261.651219	-261.124143	-260.109464
0.0	-261.911181	-260.767543	-261.121765	-260.451033
-0.25	-259.138174	-261.101621	-261.171572	-260.888128
b / a	-0.25	0.0	0.25	0.5

Table 3-6 Total energy of the various choices of lateral matching with NiGe(112)T8 and Ge(001) slabs.

0.5	-260.378385	-260.987493	-261.120540	-260.391306
0.25	-260.121467	-260.372227	-260.486646	-260.913642
0.0	-260.233243	-261.124734	-260.931925	-260.269548
-0.25	-261.128308	-261.663801	-260.240347	-260.977027
b / a	-0.25	0.0	0.25	0.5

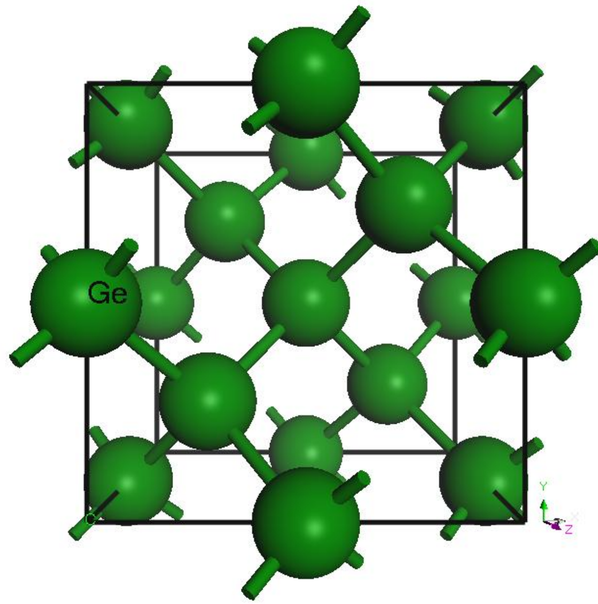

Figure 3-1 Conventional cell of the Ge bulk.

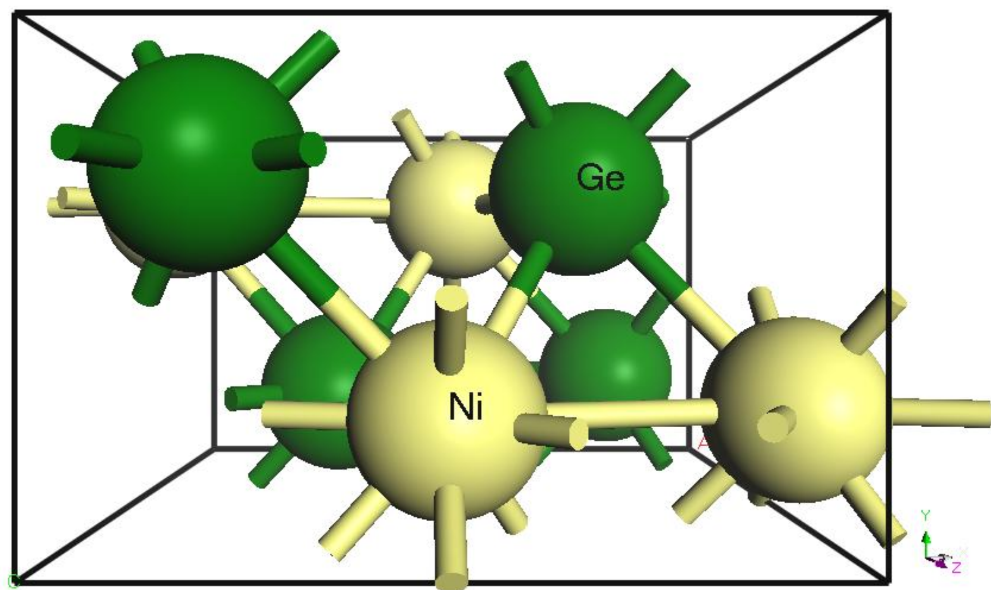

Figure 3-2 Atomic structure of the NiGe bulk.

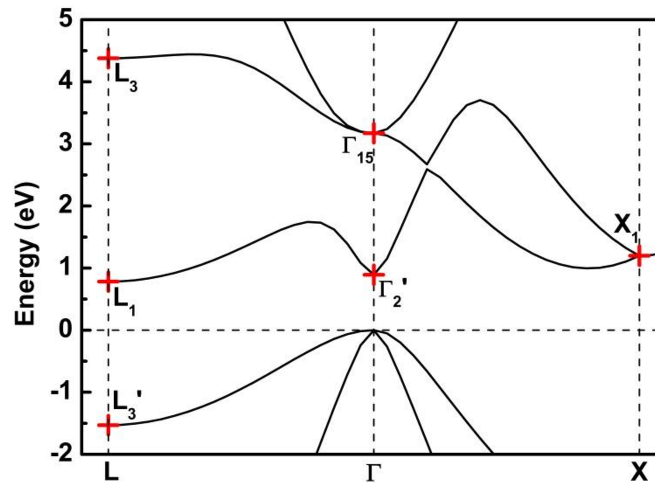

Figure 3-3 Calculated band structure of the Ge bulk by HSE06. The red crosses stand for the high-symmetry points as measured by thr photoemission experiments. The enerygy reference is set at the Fermi-level.

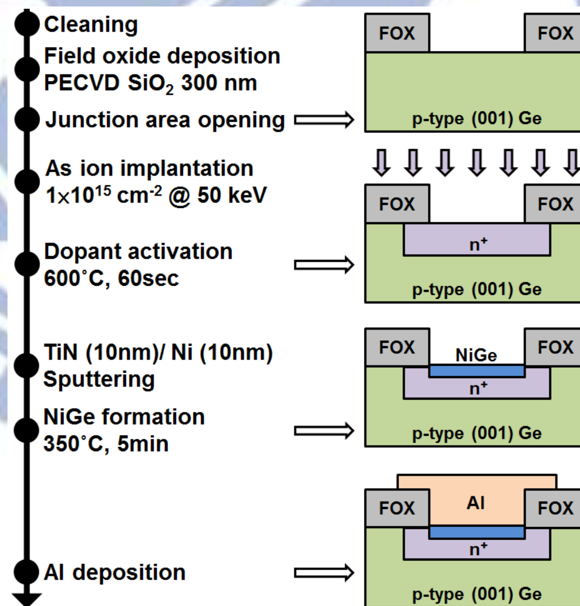

Figure 3-4 Process flow of the self-aligned NiGe n^+/p junction.

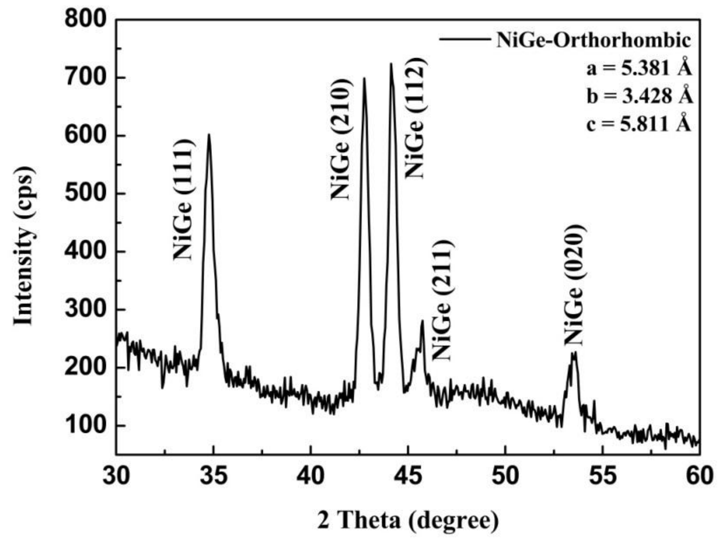

Figure 3-5 X-ray diffraction (XRD) sprectrum of the NiGe/Ge structure formed by 350°C annealing shows polycrystalline NiGe phases.

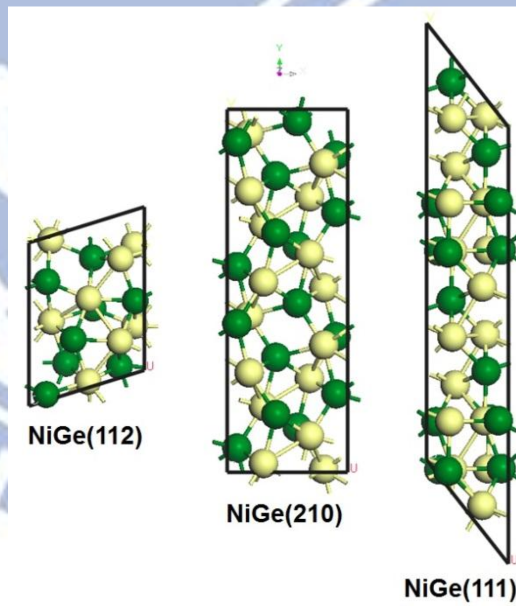

Figure 3-6 Lateral cell shape of the NiGe(112), (210), and (111) slabs on the Ge(001) surface.

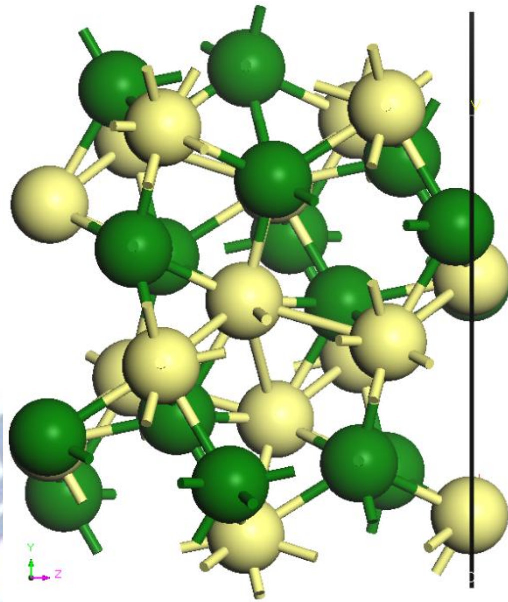

Figure 3-7 One of the surface terminations of the NiGe(112) slab, called NiGe(112)T4 slab, contains 4 atoms (2 Ni and 2 Ge atoms) per lateral unit cell.

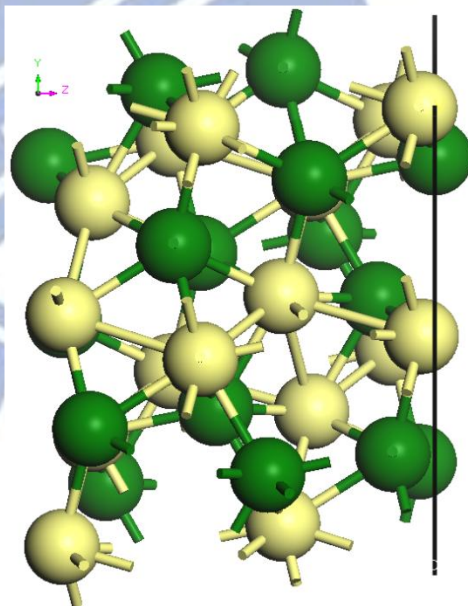

Figure 3-8 One of the surface terminations of the NiGe(112) slab, called NiGe(112)T8 slab, contains 8 atoms (4 Ni and 4 Ge atoms) per lateral unit cell.

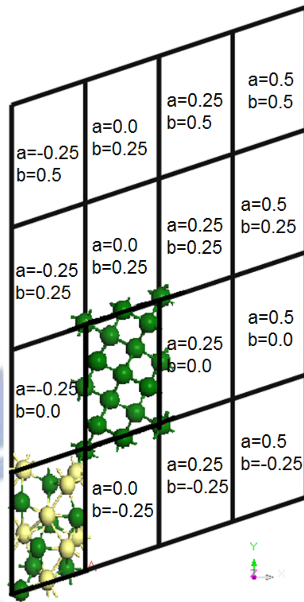

Figure 3-9 Various choices of lateral matching of the NiGe(112) and Ge(001) slab. The a and b stand for the origin offset of the NiGe slab at x and y direction, respectively.

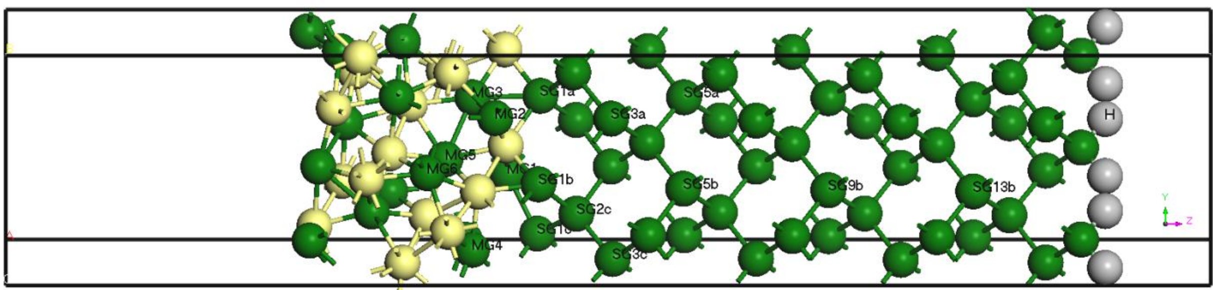

Figure 3-10 Atomic structure of the NiGe/Ge contact.

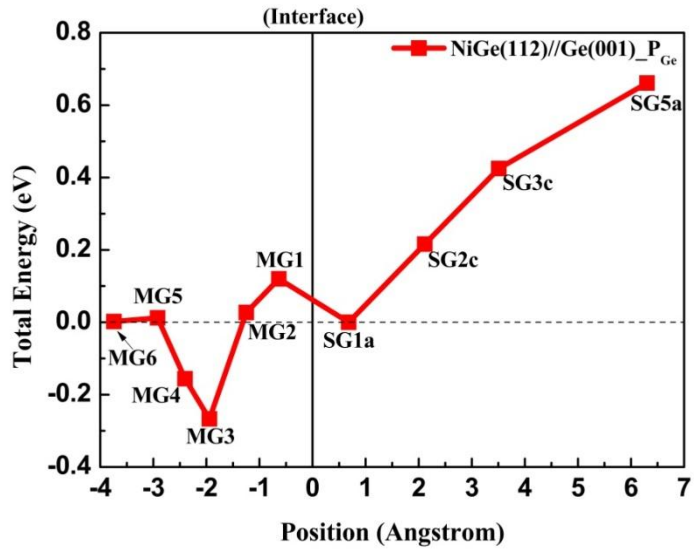

Figure 3-11 Total energy of the NiGe/Ge interface structure with one Ge atom being substituted for a phosphorous, where the energy reference is taken to be the cases with the most left substitutional sites.

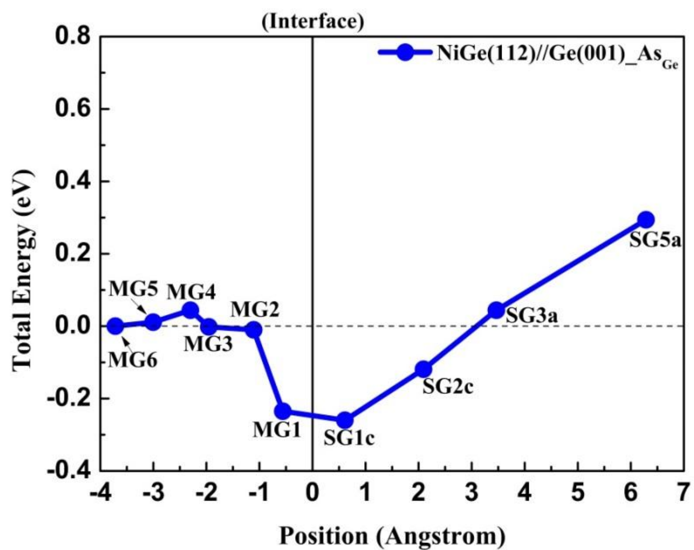

Figure 3-12 Total energy of the NiGe/Ge interface structure with one Ge atom being substituted for an arsenic, where the energy reference is taken to be the cases with the most left substitutional sites.

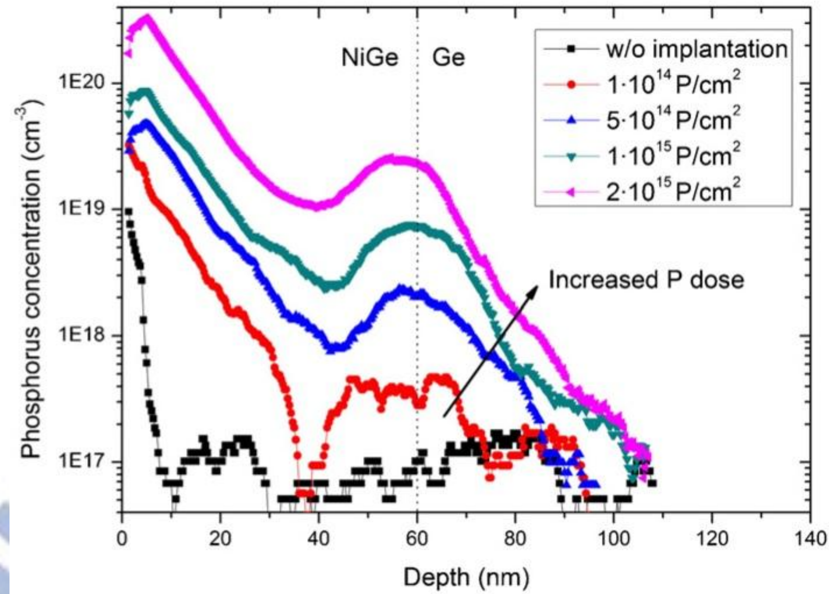

Figure 3-13 Secondary ion mass spetroscopic (SIMS) profiles shows the phosphorous segregation at the NiGe/Ge(001) interface with a NiGe thickness of 60 nm [23].

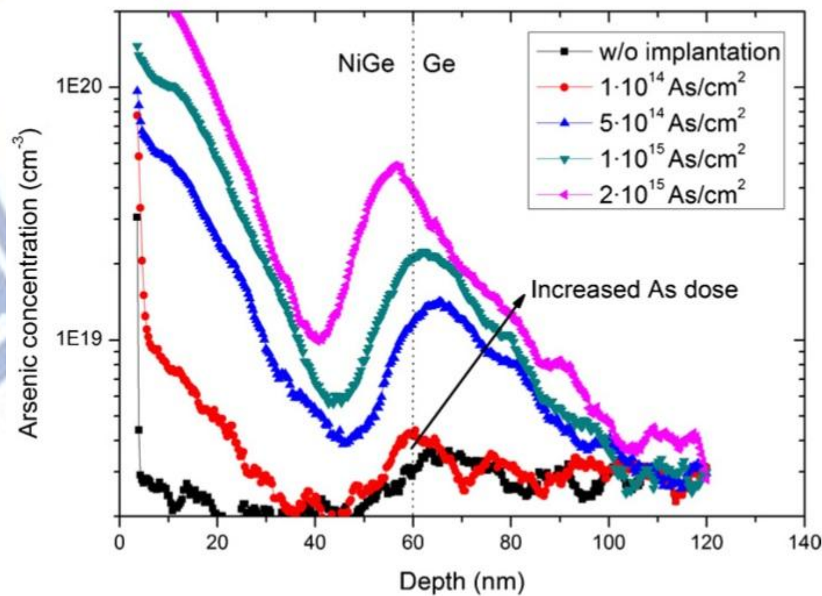

Figure 3-14 Secondary ion mass spetroscopic (SIMS) profiles shows the arsenic segregation at the NiGe/Ge(001) interface with a NiGe thickness of 60 nm [23].

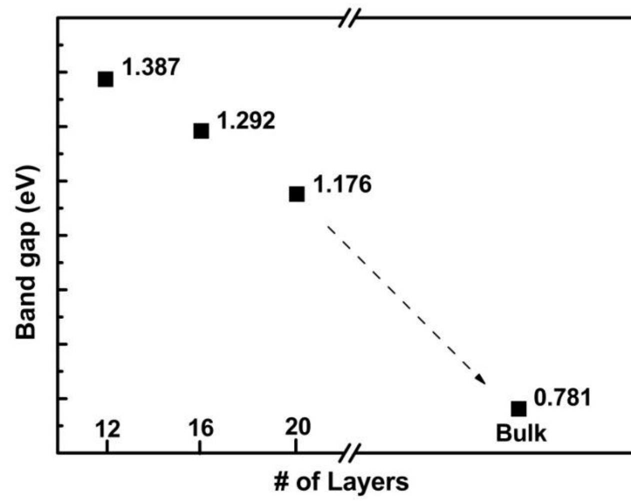

Figure 3-15 Bandgap of the Ge(001) slab as a function of the nuber of atomic layers.

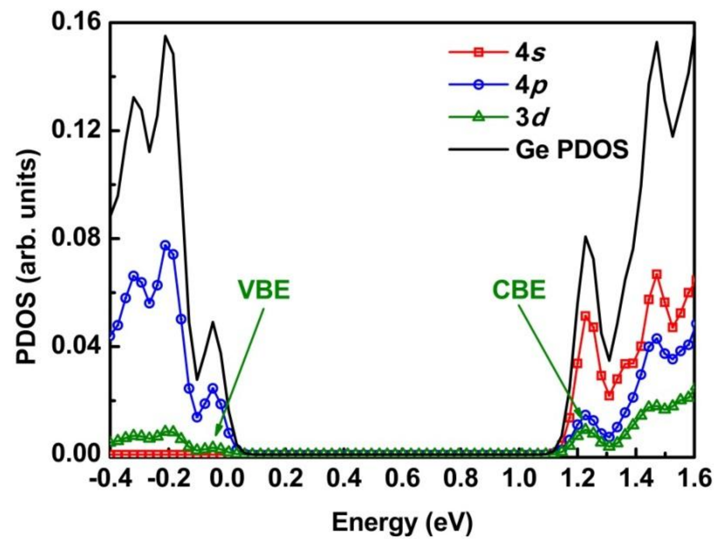

Figure 3-16 Partial density of states (PDOS) of the Ge atom in the pure 16-layers Ge(001) slab.

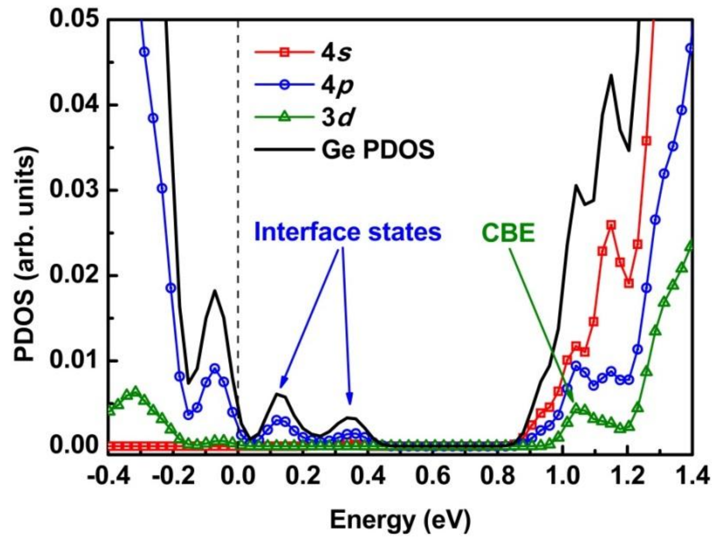

Figure 3-17 Partial density of states (PDOS) of the Ge atom labeled as SG9b (see Figure 3-10) in the undoped NiGe/Ge interfacial structure.

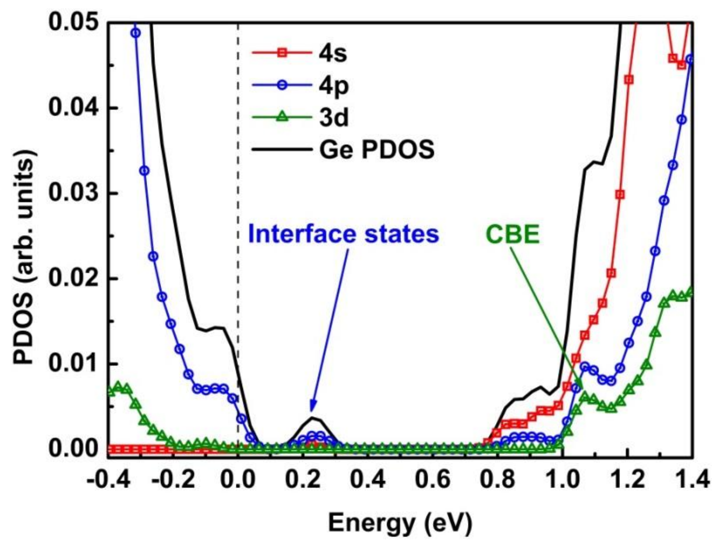

Figure 3-18 Partial density of states (PDOS) of the Ge atom labeled as SG9b (see Figure 3-10) in the NiGe/Ge interface structure when doping phosphorous at the most stable position.

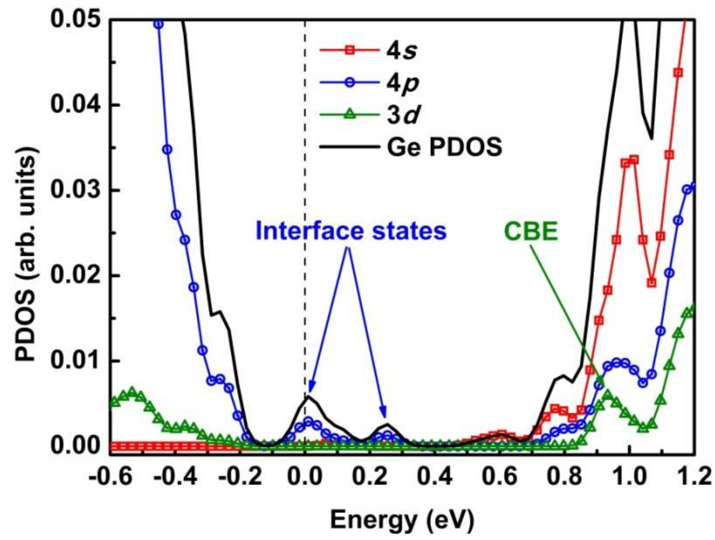

Figure 3-19 Partial density of states (PDOS) of the Ge atom labeled as SG9b (see Figure 3-10) in the NiGe/Ge interface structure when doping phosphorous at the metastable site.

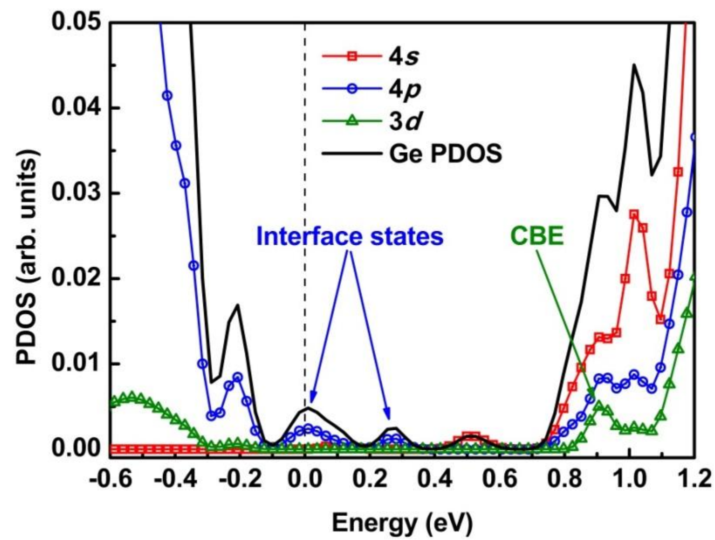

Figure 3-20 Partial density of states (PDOS) of the Ge atom labeled as SG9b (see Figure 3-10) in the NiGe/Ge interface structure when doping arsenic at the most stable position.

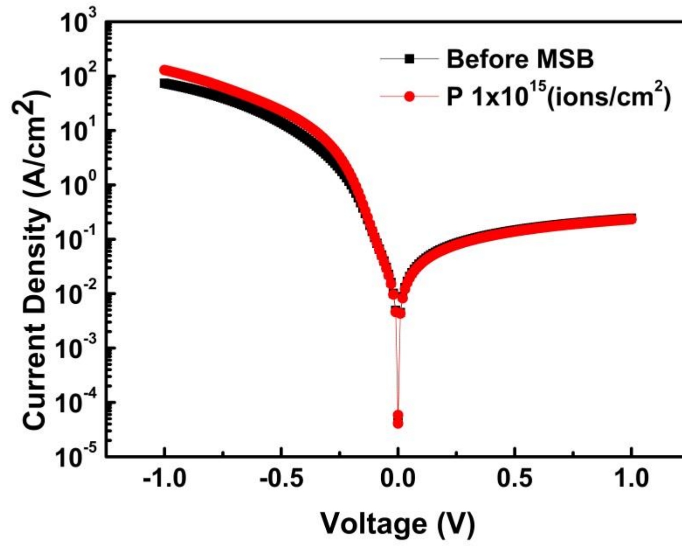

Figure 3-21 Current-voltage characteristics of the NiGe/Ge junction without and with phosphorous segregation [44].

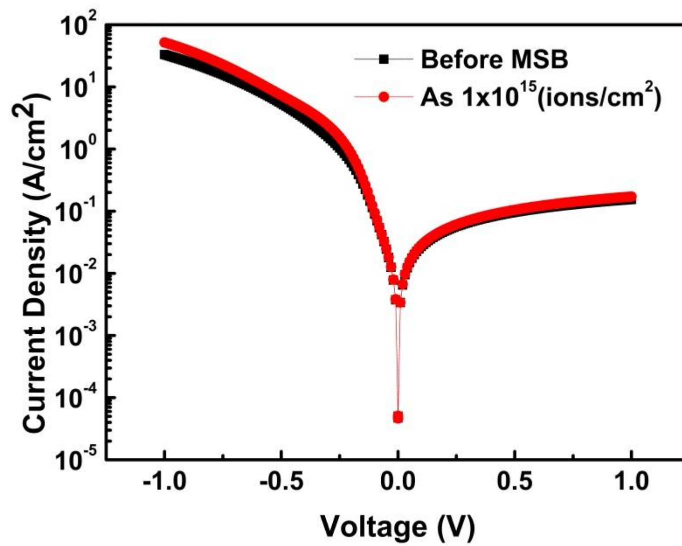

Figure 3-22 Current-voltage characteristics of the NiGe/Ge junction without and with arsenic segregation [44].

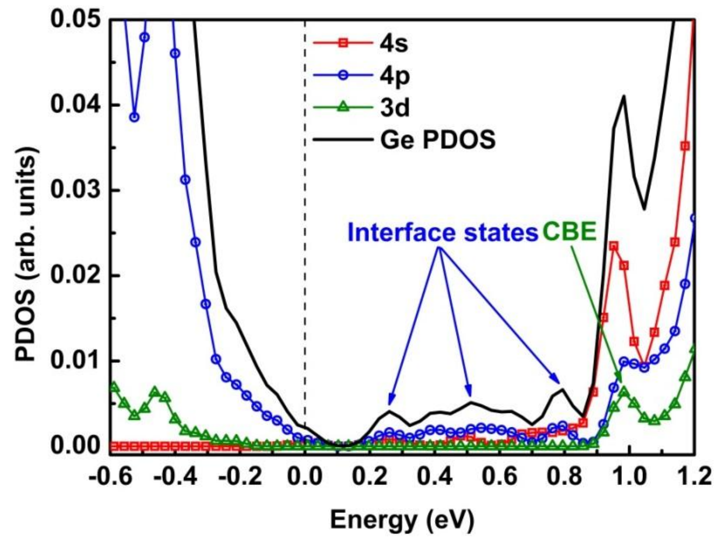

Figure 3-23 Partial density of states (PDOS) of the Ge atom labeled as SG9b (see Figure 3-10) in the NiGe/Ge interface structure when doping nitrogen at the most stable position.

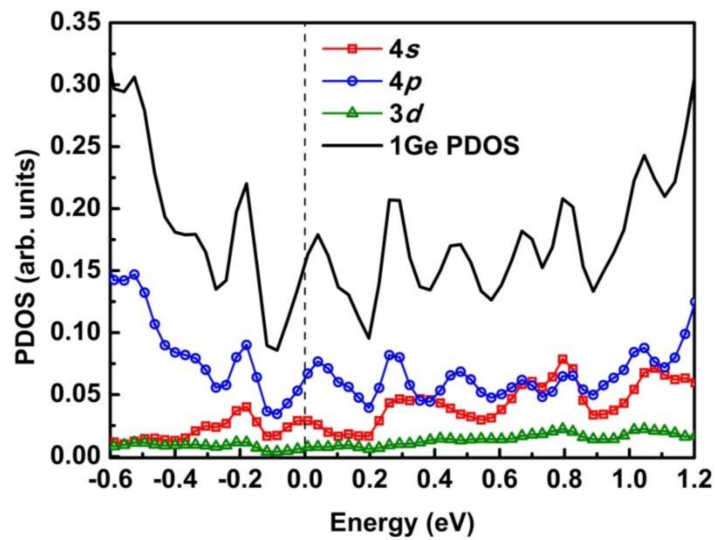

Figure 3-24 Partial density of states (PDOS) of the Ge atom labeled as SG1b (see Figure 3-10) in the NiGe/Ge interface structure when doping nitrogen at the most stable position.

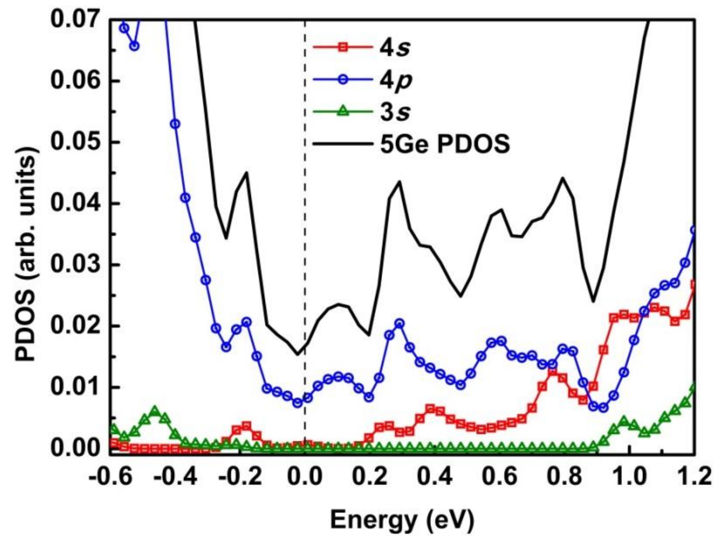

Figure 3-25 Partial density of states (PDOS) of the Ge atom labeled as SG5b (see Figure 3-10) in the NiGe/Ge interface structure when doping nitrogen at the most stable position.

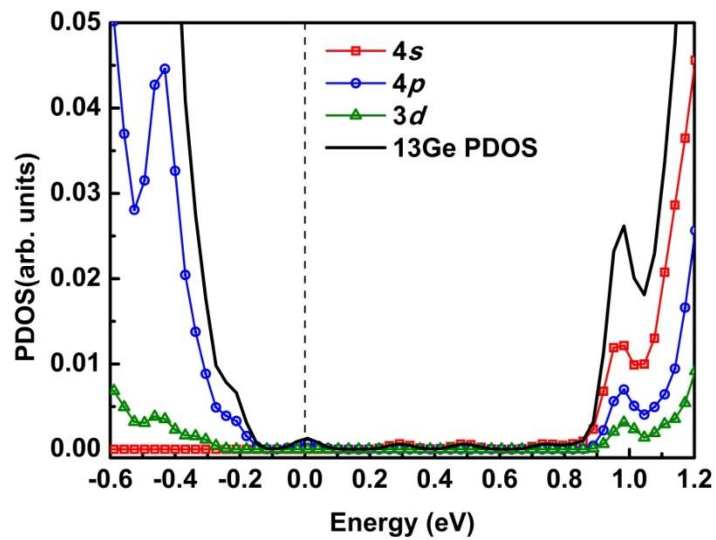

Figure 3-26 Partial density of states (PDOS) of the Ge atom labeled as SG13b (see Figure 3-10) in the NiGe/Ge interface structure when doping nitrogen at the most stable position.

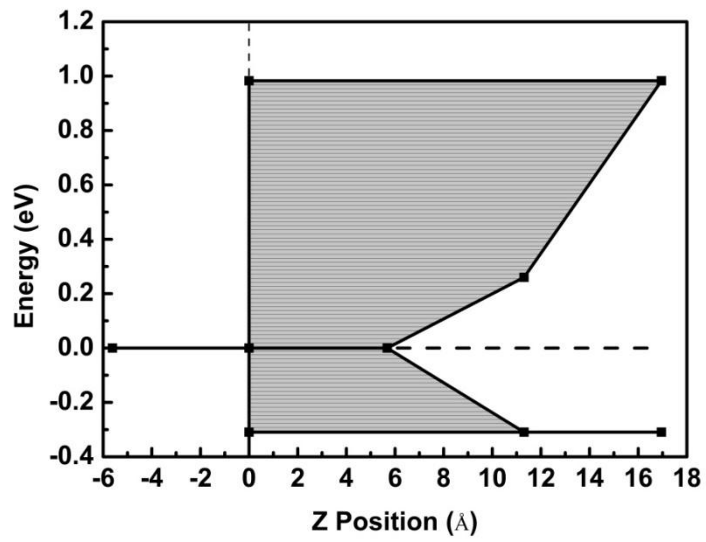

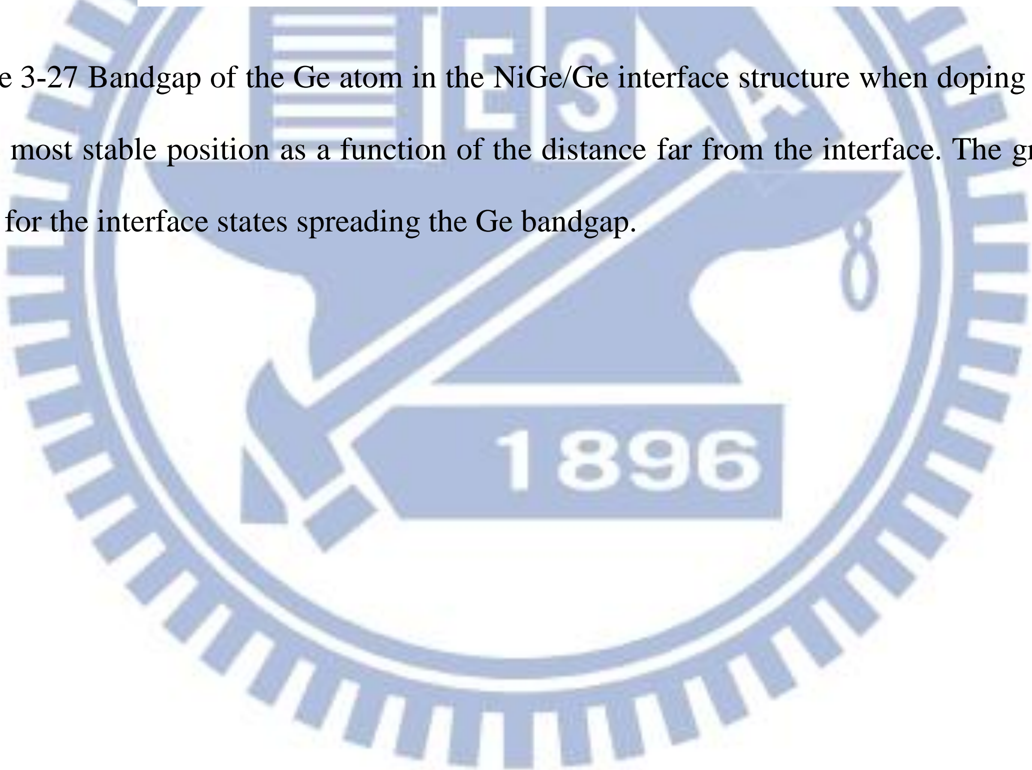

Figure 3-27 Bandgap of the Ge atom in the NiGe/Ge interface structure when doping nitrogen at the most stable position as a function of the distance far from the interface. The gray lines stand for the interface states spreading the Ge bandgap.

Chapter 4 Conclusion and Future works

4.1 Conclusions

In this thesis, the effect of dopant segregation on the NiGe/n-Ge contact is studied by first-principles calculations. We show that the calculated lattice constant, a=5.645Å, using the LDA exchange-correlation functional is closest to the experimental value a=5.658Å. Using this calculated lattice constant, we figure out that HSE06 is the only exchange-correlation functional that can give rise to a correct Ge bandgap, 0.781 eV as well as the dispersions at the high-symmetry points that agree excellently with the experiment. Consequently, we use LDA functional to relax the atomic structures and then use HSE06 hybrid functional to calculate the electronic structures throughout the rest of this thesis.

Then, we build the atomic structure of the NiGe/Ge contact according to our experimental sample, which is grown by sputtering 10-nm-thick Ni on the lightly-doped n-type Ge region and annealing at 350°C for 5 minutes by a backend vacuum annealing furnace to form germanide. The XRD diffraction spectrum of this NiGe/Ge contact shows that the NiGe film has polycrystalline phases and is composed of NiGe (112), (210), and (111) orientations mainly. In order to simplify the theoretical calculations, we use merely the highest XRD peak, the (112) orientation, to represent the polycrystalline NiGe film. Therefore, the NiGe/Ge contact is simulated by a supercell of 8 NiGe (112) layers, 16 Ge (001) layers, and 12-Å vacuum where the dangling bonds of the Ge surface is saturated by H atoms. We show that the NiGe/Ge contact becomes the most stable when the cleaving surface of the NiGe slab contain only 4 atoms (2 Ni and 2 Ge atoms) with the Ni of NiGe slab being matched to the Ge of Ge slab.

Our first-principles calculations conclude that phosphorous and arsenic may segregate at the interface, but the preferred segregation position of phosphorous and arsenic are at the NiGe side and Ge side, respectively. These results imply that phosphorous would be a better choice for IBG process to increase higher dopant concentration at the interface, while arsenic atoms can migrate into the Ge layer and pile up at the interface in both IAG and IBG process.

We show that the physical Schottky barrier height of the NiGe/Ge contact modified by dopant segregation using conventional n-type dopant such as phosphorous and arsenic on the Ge side is not very effective. The energy difference between the Fermi level and the physical conduction band edge is reduced less than 0.1 eV in both cases since the Fermi level is pinned by the interface states near the valence band edge. Additionally, we also find out that there is no effect to modify the physical Schottky barrier height by doping phosphorous at the NiGe side. The Fermi level does not change by substituting phosphorous for Ge atom of the metallic Ni-Ge bond since no additional valence electron is yielded to occupy higher states. To sum up, the improvement of the NiGe/n-type Ge junction characteristics by dopant segregation using phosphorous and arsenic are mainly attributed to the increase of dopant concentration around the interface and insignificantly attributed to the reduction of the physical Schottky barrier height.

Finally, we study the effects of nitrogen segregation at the NiGe/Ge interface. The results show that the nitrogen dopant can be segregated around the interface and give a large number of the interface states spreading the Ge bandgap. Although the effective conduction band edge is closer to the Fermi level due to the broadening interface states, but the interface states disappear beyond 17Å away from the interface. Therefore, the physical Schottky barrier height of electrons is almost unchanged by dopant segregation using nitrogen dopant.

4.2 Future Works

We understand that Schottky barrier height of the NiGe/Ge contact modified by dopant segregation is not very effective arising from a great quantity of interface states near the valence band edge. How to decrease the interface states becomes a crucial task to increase the effect of the dopant segregation. Nevertheless, the mechanism of reduction the interface state is still unclear through our first-principles calculations. Therefore, we will calculate some doping element such as scandium, titanium, vanadium, and sulfur around the NiGe/Ge interface to investigate whether the interface states can be reduced by the above-mentioned dopant elements.

Since the DFT plane-wave calculations using the HSE06 hybrid functional is too expensive to calculate the large spuercells of the NiGe/Ge contact, the wavefunction must be represented in more efficient basis sets for example, the linear combination of atomic orbitals.

In order to be compared with the current-voltage characteristics, we will apply non-equilibrium Green's function (NEGF) method to further compute the transport properties out of calculated electronic structures, where NEGF can be easily extended to finite temperature.

References

[1] G. E. Moore, "Cramming more components onto integrated circuits," *Electronics*, vol. 38, no. 8, pp. 114-117, 1965.

[2] A. M. Noori, M. Balseanu, P. Boelen, A. Cockburn, S. Demuynck, S. Felch, S. Gandikota, A. J. Gelatos, A. Khandelwal, J. A. Kittl, A. Lauwers, W.-C. Lee, J. Lei, T. Mandrekar, R. Schreutelkamp, K. Shah, S. E. Thompson, P. Verheyen, C.-Y. Wang, L.-Q. Xia, and R. Arghavani, "Manufacturable Processes for ≤ 32-nm-node CMOS Enhancement by Synchronous Optimization of Strain-Engineered Channel and External Parasitic Resistances" *IEEE Trans. Electron Devices,* vol. 55, pp. 1259-1264, 2008.

[3] S.-D. Kim, C.-M. Park, and J. C. Woo, "Advanced model and analysis of series resistance for CMOS scaling into nanometer regime. I. Theoretical derivation," *IEEE Trans. Electron Devices,* vol. 49, pp. 457-466, 2002.

[4] S.-D. Kim, C.-M. Park, and J. C. Woo, "Advanced model and analysis of series resistance for CMOS scaling into nanometer regime. II. Quantitative analysis," *IEEE Trans. Electron Devices,* vol. 49, pp. 467-472, 2002.

[5] B. Sharma, *Metal-semiconductor Schottky barrier junctions and their applications*, New York: Plenum Press, pp. 2-8, 1984.

[6] W. Mönch, *Electronic properties of semiconductor interfaces*, Springer, pp.4-7, 2004.

[7] J. Bardeen, "Surface states and rectification at a metal semi-conductor contact," *Phys. Rev.,* vol. 71, p. 717, 1947.

[8] E. H. Rhoderick and R. Williams, *Metal-semiconductor contacts*, Oxford: Clarendon Press, pp. 90-117, 1988.

[9] T. Ghani, M. Armstrong, C. Auth, M. Bost, P. Charvat, G. Glass, T. Hoffmann, K. Johnson, C. Kenyon, J. Klaus, B. Mclntyre, K. Mistry, A. Murthy, J. Sandford, M. Silberstein, S. Sivakumar, P. Smith, K. Zawadzki, S. Thompson, and M. Bohr, "A 90nm high volume manufacturing logic technology featuring novel 45nm gate length strained silicon CMOS transistors," in *IEDM Tech. Dig.*, 2003, pp. 11.6. 1-11.6. 3.

[10] Y. Kamata, "High-k/Ge MOSFETs for future nanoelectronics," *Mater. Today,* vol. 11, pp. 30-38, 2008.

[11] E. Simoen, A. Satta, A. D’Amore, T. Janssens, T. Clarysse, K. Martens, B. D. Jaeger, A. Benedetti, I. Hoflijk, B. Brijs, M. Meuris, and W. Vandervorst, "Ion-implantation issues in the formation of shallow junctions in germanium," *Mater. Sci. Semicond. Process.,* vol. 9, pp. 634-639, 2006.

[12] H. Shang, H. Okorn-Schmidt, K. K. Chan, M. Copel, J. A. Ott, P. Kozlowski, S. E. Steen, S. A. Cordes, H.-S. P. Wong, E. C. Jones and W. E. Haensch, "High mobility p-channel germanium MOSFETs with a thin Ge oxynitride gate dielectric," in *IEDM Tech. Dig.*, 2002, pp. 441-444.

[13] F. A. Trumbore, "Solid Solubilities of impurity elements in germanium and silicon" *Bell Syst. Tech. J,* vol. 39, pp. 205-233, 1960.

[14] E. Simoen and J. Vanhellemont, "On the diffusion and activation of ion-implanted n-type dopants in germanium," *J. Appl. Phys.,* vol. 106, pp. 103516-103516-4, 2009.

[15] C. O. Chui, K. Gopalakrishnan, P. B. Griffin, J. D. Plummer, and K. C. Saraswat, "Activation and diffusion studies of ion-implanted p and n dopants in germanium," *Appl. Phys. Lett.,* vol. 83, pp. 3275-3277, 2003.

[16] C. O. Chui, L. Kulig, J. Moran, W. Tsai, and K. C. Saraswat, "Germanium n-type shallow junction activation dependences," *Appl. Phys. Lett.,* vol. 87, pp. 091909-091909-3, 2005.

[17] P. Tsouroutas, D. Tsoukalas, I. Zergioti, N. Cherkashin, and A. Claverie, "Diffusion and activation of phosphorus in germanium," *Mater. Sci. Semicond. Process.,* vol. 11, pp. 372-377, 2008.

[18] T. Liu and M. Orlowski, "Arsenic diffusion in boron-doped germanium," *Electron. Lett.,* vol. 49, pp. 154-156, 2013.

[19] C.-C. Wang, C.-J. Lin, and M.-C. Chen, "Formation of NiSi-Silicided p+ n Shallow Junctions Using Implant-Through-Silicide and Low-Temperature Furnace Annealing," *J. Electrochem. Soc.,* vol. 150, pp. G557-G562, 2003.

[20] C.-P. Lin, Y.-H. Xiao, and B.-Y. Tsui, "High-performance poly-Si TFTs fabricated by implant-to-silicide technique," *IEEE Electron Device Lett.,* vol. 26, pp. 185-187, 2005.

[21] Q. Zhao, U. Breuer, E. Rije, and S. Mantl, "Tuning of NiSi / Si Schottky barrier heights by sulfur segregation during Ni silicidation," *Appl. Phys. Lett.,* vol. 86, p. 062108, 2005.

[22] N. Mise, S. Migita, Y. Watanabe, H. Satake, T. Nabatame, and A. Toriumi, "(111)-Faceted Metal Source and Drain for Aggressively Scaled Metal/High-k MISFETs," *IEEE Trans. Electron Devices,* vol. 55, pp. 1244-1249, 2008.

[23] M. Mueller, Q. Zhao, C. Urban, C. Sandow, D. Buca, S. Lenk, S. Lenk, S. Estévez, S. Mantl, "Schottky-barrier height tuning of NiGe/n-Ge contacts using As and P segregation," *Mater. Sci. Eng., B,* vol. 154, pp. 168-171, 2008.

[24] Y. Tada, K. Suzuki, and Y. Kataoka, "High-precision Evaluation of Ultra-shallow Impurity Profiles by Secondary Ion Mass Spectrometry," *Sci. Tech. J.*, vol. 46, no. 3, 2010.

[25] International Technology Roadmap for Semiconductor, 2012 Edition, Semiconductor Industry Association: San Jose, CA, 2012.

[26] M. K. Niranjan, "Theoretical investigation of contact materials for emerging electronic and spintronic devices," Ph.D Thesis, Department of Physics, The University of Texas at Austin, 2007.

[27] R. M. Martin, Electronic structure: basic theory and practical methods, Cambridge university press, pp. 52-67, 2004.

[28] D. R. Hartree, "The wave mechanics of an atom with a non-Coulomb central field. Part I. Theory and methods," in *Math. Proc. Cambridge*, 1928, pp. 89-110.

[29] D. R. Hartree, "The wave mechanics of an atom with a non-coulomb central field. Part II. Some results and discussion," in *Math. Proc. Cambridge*, 1928, pp. 111-132.

[30] D. Hartree, "The wave mechanics of an atom with a non-coulomb central field. Part III. Term values and intensities in series in optical spectra," in *Math. Proc. Cambridge*, 1928 ,pp. 426-437.

[31] P. Hohenberg and W. Kohn, "Inhomogeneous electron gas," *Phys. Rev.,* vol. 136, p. B864, 1964.

[32] W. Kohn and L. J. Sham, "Self-consistent equations including exchange and correlation effects," *Phys. Rev.,* vol. 140, p. A1133, 1965.

[33] P. A. M. Dirac, "Quantum mechanics of many-electron systems," *Proc. R. Soc. London. Ser. A,* vol. 123, pp. 714-733, 1929.

[34] D. Ceperley and B. Alder, "Ground state of solid hydrogen at high pressures," *Phys.*

Rev. B, vol. 36, p. 2092, 1987.

[35] J. P. Perdew and A. Zunger, "Self-interaction correction to density-functional approximations for many-electron systems," *Phys. Rev. B,* vol. 23, p. 5048, 1981.

[36] J. P. Perdew, "Accurate density functional for the energy: Real-space cutoff of the gradient expansion for the exchange hole," *Phys. Rev. Lett.,* vol. 55, p. 1665, 1985.

[37] J. P. Perdew and Y. Wang, "Accurate and simple analytic representation of the electron-gas correlation energy," *Phys. Rev. B,* vol. 45, p. 13244, 1992.

[38] J. P. Perdew, K. Burke, and M. Ernzerhof, "Generalized gradient approximation made simple," *Phys. Rev. Lett.,* vol. 77, p. 3865, 1996.

[39] J. Heyd, G. E. Scuseria, and M. Ernzerhof, "Erratum:"Hybrid functionals based on a screened Coulomb potential"[J. Chem. Phys. 118, 8207 (2003)]," *J. Chem. Phys.,* vol. 124, pp. 219906-219906-1, 2006.

[40] J. P. Perdew, M. Ernzerhof, and K. Burke, "Rationale for mixing exact exchange with density functional approximations," *J. Chem. Phys.,* vol. 105, p. 9982, 1996.

[41] D. Ceperley and B. Alder, "Exchange-correlation potential and energy for density-functional calculation," *Phys. Rev. Lett.,* vol. 45, pp. 567-581, 1980.

[42] O. Madelung, Semiconductors: data handbook, Berlin: Springer, p. 46, 2004.

[43] Y. Chen and U. Ravaioli, "Band Structure Calculation of Si and Ge by Non-Local Empirical Pseudo-Potential Technique," J. Electron. Sci. Technol. China, vol. 3, no.1, pp. 52-56, 2005.

[44] C.-J. Shih, "A Study on the Nickel Germanide Contacted N+-P Germanium Shallow Junction and Contact Resistance," Master thesis, Department of Electronics Engineering and Institute of Electronics, National Chiao Tung University, 2013.

[45] T. H. Phung, R. Xie, S. Tripathy, M. Yu, and C. Zhu, "Low Temperature Metal Induced Lateral Crystallization of Ge Using Germanide Forming Metals," *J. Electrochem. Soc.,* vol. 157, pp. H208-H213, 2010.

[46] Q. Gao and J. Guo, "Barrier height determination of silicide-silicon contact by hybrid density functional simulation," *Appl. Phys. Lett.,* vol. 99, pp. 183110-183110-3, 2011.

Author's Biography

姓名: 林翰奇

性別: 男

生日: 民國 78 年 8 月 30 日

學歷:

高雄市立十全國民小學 (84.9-90.6)

高雄市立三民國民中學 (90.9-93.6)

國立鳳山高級中學 (93.9-96.6)

國立中興大學物理學系 (96.9-100.6)

國立交通大學電子研究所固態組碩士 (100.9-102.9)

碩士論文題目:

鎳鍺化物與N型鍺接面摻雜析離對於蕭基位障的影響:透過第一原理計算

Schottky Barrier Height of the NiGe/n-type Ge Contact with Dopant Segregation: A First-principles Study